Calibrating and adapting a deterministic proton transport algorithm to perform patient-specific quality assurance

E. J. M. Benschop

TU Delft

Calibrating and adapting a deterministic proton transport algorithm to perform patient-specific quality assurance

by

E. J. M. Benschop

to obtain the degree of Master of Science
at the Delft University of Technology,
to be defended publicly on Friday June 7, 2024 at 9:00 AM.

Student number:	5132118	
Project duration:	September 4, 2023 – June 7, 2024	
Thesis committee:	Dr. Z. Perkó,	TU Delft, thesis supervisor
	T. Burlacu,	TU Delft, daily supervisor
	Dr. Ir. D. Lathouwers,	TU Delft
	Dr. Ir. A. Denkova,	TU Delft

Cover: Proton therapy gantry from https://HollandPTC.nl (2024)

TU Delft

Abstract

To reduce the probability of complications in proton therapy, while maintaining a high tumor control probability, adaptive treatment can be applied. In adaptive treatments, the treatment plans are frequently assessed and adjusted to, for example, account for anatomical changes. Ideally, daily adaptive treatment would be implemented, where every day a repeat scan is made and the treatment plan is adjusted. However, due to computational limitations, daily adaptive treatment is not possible yet. Quality assurance (QA) is a vital part of the proton therapy workflow. Intending to implement daily adaptive treatment, fast-working quality assurance tools are necessary. The goal of this thesis is to calibrate and adapt a deterministic proton transport algorithm to reconstruct the delivered dose using log files, which can be compared to the planned dose as a QA tool.

To achieve this, Yet anOther Dose Algorithm (YODA) was calibrated to the popular planning software RayStation, by optimizing the input parameters of YODA to minimize the difference in dose between YODA and RayStation for a 0° gantry angle single spot in a homogeneous water phantom. From this calibration, beam data library (BDL) files were created for cases without a range shifter and with range shifters of thicknesses 2 cm, 3 cm and 5 cm and planned spot energies ranging from 70 MeV to 190 MeV. An approximation to improve the inclusion of the effect of nuclear interactions was added to YODA. The lowest passing rate found was 99.47% for a 190 MeV spot without a range shifter, therefore the calibration was successful. The passing rate decreased for high energies, likely due to the crude approximation to deal with nuclear interactions. Other ways to include the effect of nuclear interaction should be investigated to further improve the calibration results. After the calibration was complete, three experiments were performed.

First, simple treatment plan comparisons were performed using the BDL files and a homogeneous water phantom, including plans containing a single spot irradiated from gantry angles ranging from 10° to 90°. To account for the angled beams, a beam splitting algorithm was used. It was observed that the BDL files are specific for the isocenter to CT volume surface distance, as the boundary conditions of YODA are at the CT volume surface while the treatment plans define spots at the isocenter in air. To include this effect, the BDLs should contain beamlet parameters at the isocenter, from which the beamlet parameters at the CT volume surface can be calculated. The calibration procedure for the spatial spread, angular spread and correlation needs to be adjusted. Alternatives to the beam splitting algorithm should be investigated, as this algorithm inadequately reflects reality when a beam enters the CT volume under an angle.

Second, YODA assumes that spots are laterally symmetrical, however, in reality, spots are ellipse-shaped. To solve this, the asymmetrical spot solution to the Fermi-Eyges equation was derived. The difference in integrated Fermi-Eyges flux between the symmetrical and asymmetrical spot was calculated for realistic combinations of lateral spread, angular spread and correlation. The mean error in integrated Fermi-Eyges flux, relative to the maximum, induced by assuming lateral spot symmetry, around the central beam axis is significant, as it ranges from 0.6853% to 3.071% at the entrance of the CT volume and from 0.4710% to 4.957% at the Bragg peak. Therefore the asymmetrical spot solution should be implemented, after which, YODA should be re-calibrated

Third, the error induced by systematic errors in the log file was investigated. The plan contains a target cube centered in the homogeneous water phantom irradiated by a 0° gantry angle beam. By perturbing each energy layer randomly using a uniform distribution, where the maximum perturbation was 0.8 mm in spot position, 1% for MU and 0.1% for energy, the magnitude of the dose difference was calculated. The mean differences in dose in the target cube induced by randomly perturbing each energy layer were $0.1204\% \pm 0.0408\%$ in x, $0.1700\% \pm 0.0324\%$ in z, $0.2592\% \pm 0.1595\%$ in MU and $0.4802\% \pm 0.1558\%$ in energy. These differences are small compared to the error induced by assuming symmetrical spots, note that the differences in spatial spread were an order of magnitude bigger than the perturbation in spot position. Before this investigation on the effect of systematic errors can continue, the asymmetrical spot solution needs to be implemented and the problems discovered with angled beams should be solved.

The calibration was successful, and additional extensions and alterations have been identified to further improve YODA before it can be used as the described patient-specific quality assurance tool.

Contents

List of Figures

List of Tables

1

Introduction

In this chapter, the background of proton therapy, quality assurance and the deterministic proton algorithm will be introduced and discussed. Then the research question will be formulated and divided into sub-questions.

1.1. Proton therapy background

According to the Dutch Cancer Foundation, KWF, one in three people gets diagnosed with cancer in their lifetime, with a 65% five-year survival chance [1]. There are a few commonly used treatment modalities, for example, surgery or chemotherapy. Another well-established treatment modality for cancer is radiotherapy (RT). Ionizing radiation is used to damage the DNA of tumor cells, where a certain dose with the unit Gray (Gy) is prescribed to the patient. External radiotherapy is a modality where the source of the radiation is outside the patient and there are two common forms of external radiotherapy: photon therapy and proton therapy. The dose-depth characteristics of a photon beam, illustrated in Figure 1.1, show first a build-up region, then a peak and a gradual decline in dose.

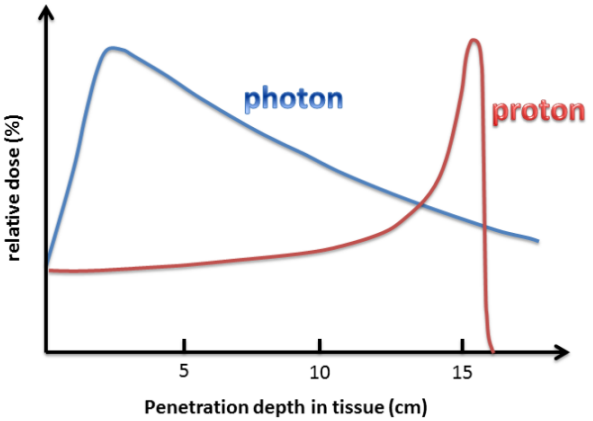

Figure 1.1: Schematic graph of depth dose curve of photon (in blue) and proton (in red) beam. Adapted from Zhang [2].

Proton therapy has a low entrance and a negligible exit dose due to the steep Bragg peak [3] as shown in Figure 1.1. This causes proton therapy to be able to deliver a high dose to the tumor while minimizing damage to the healthy tissue [3]. However, due to this steep Bragg peak, a small displacement can cause a high dose to be placed in the healthy tissue instead of the tumor. Therefore, there is a risk of tumor underdosage, which increases the patient's mortality chances, and a risk of healthy tissue overdosage, which increases the probability of complications [4]. The current standard radiotherapy workflow involves creating a treatment plan based on a single computed tomography (CT) image [5]. The plan is optimized to have a high tumor control probability and a low complication probability. To account for uncertainties in the treatment, robust optimization is used,

where uncertainty models are considered in the optimization so that the resulting plan performs well under most scenarios within the boundaries of the uncertainty models [5]. This leads to a margin around the tumor that is also irradiated however, this margin is smaller than a margin that results from uniformly expanding around the tumor to account for uncertainties. This plan is then administered in multiple fractions of lower doses to help the healthy tissue recover while still damaging the tumor tissue enough to eliminate it [4].

During the treatment, there are unpredictable anatomical changes in the patient that can not be taken into account in the initial treatment planning. Some of these changes include for example weight loss or the shrinkage of the tumor [5]. Another downside to the current treatment procedure is the use of the margins resulting for robust optimization. Although these margins help to account for uncertainties, this approach also results in a higher dose to the healthy tissue within the margin. To take these anatomical changes into consideration, the treatment plan should be reevaluated and recalculated after administering a certain amount of fractions. This is called adaptive therapy. The goal of adaptive therapy is to deliver the prescribed dose to the tumor while sparing healthy tissue despite anatomical changes to the patient during the treatment [5]. Since radiotherapy is fractionated, the treatment plan can be adapted during the course of the treatment period based on the anatomy of the patient. This can reduce the margins that are radiated around the tumor, while still maintaining a high dose to the tumor and a lower complication probability [5]. The frequency of a treatment plan adaptation can differ. To account for day-to-day anatomical changes, ideally, every day an image would be made and the treatment plan would be recalculated almost in real-time based on this new image, this is called daily adaptive radiotherapy. However, the computational expense [6] and the computation time needed to re-optimize the treatment plan [7] are too large for this application, making it impossible to recalculate the plan daily.

1.2. Quality assurance

The steepness of the Bragg peak makes quality assurance (QA) a vital aspect of the treatment [8]. Quality assurance contains all procedures taken to ensure consistency of the medical prescription and the safe fulfillment of the prescription in all aspects of the treatment [4]. QA can be done in various ways, such as machine QA, where the proper functioning of the treatment system is assessed. Another example is patient-specific QA, where for every patient separately, the quality of the plan is assured using different QA tools. This can be time-consuming and therefore becomes a bottleneck in the treatment process [9]. With the goal of working towards daily adaptive treatment in mind, the QA would ideally not be a time-consuming part of the treatment.

One proposed patient specific QA tool is to compare the delivered dose to the planned dose. There can be a difference between the two dose distributions due to numerous errors and inaccuracies [10]. If the delivered dose distribution is different, this can be taken into account in the next fractions to maintain the desired clinical outcome of the treatment plan. This QA tool has been explored during the last decade.

In photon therapy, it is possible to measure the photons escaping the body with an electronic portal imaging device (EPID). Here the exiting photons are measured by a metal plate coated in phosphorous material causing fluorescence, which is caught by a camera and displayed on a monitor in real-time [11] and thus gives insight into the delivered dose to the patient. However, this is challenging with proton therapy as the protons are mostly stopped in the body. Secondary photons can be used to verify the range of the protons using the prompt gamma system. The downside of this method is that the measurement only gives insight into the range [5] and not the dose distribution. Also, detectors similar to positron emission tomography (PET) detectors are currently being investigated. The amount of secondary positrons is significantly lower than in a diagnostic PET-scan however, it is enough to create an image. The main issue with this approach is the background radiation in the room and the limited gantry angle coverage [12].

A way of reconstructing the dose would be to use log files from the proton delivery machine in combination with an independent particle transport algorithm. According to Meier et al. [9], a therapy delivery system is monitored by a build-in verification system using independent detectors. The verification system described in this publication measures and logs every pencil beam, and when they deviate from set tolerances, the treatment is interrupted. Meier et al. [9] claim that these measurements can therefore be used as a form of entrance dosimetry, and the log files can be used to reconstruct the delivered dose. Chung [3] found that the log files at Samsung Proton Therapy Center using Sumitomo Heavy Industries Ltd proton beam therapy system contain a small enough systematic error to be used for this application. Toscano et al. [13] explored the uncertainties in the log files and also concluded that if the log file uncertainties are treated correctly, the usage of log files for

QA is promising.

Meier et al. [9] have investigated the possibility of using these log files together with an independent Monte Carlo algorithm to compare the planned dose distribution to the reconstructed delivered dose distribution. Winterhalter et al. [14] have researched a similar approach using a different independent Monte Carlo-based algorithm. Both publications found that using the log files in combination with an independent Monte Carlo-based algorithm is a viable quality assurance tool. This has also been explored by Marmitt et al. [10] with another independent Monte Carlo algorithm where they compared this proposed QA tool against measurement-based QA and found that the results of both methods are consistent. Belosi et al. [8] have investigated a wider variety of tumors with this methodology and recommend that before implementing this tool in a clinical setting, first the sensitivity should be explored further.

All these results are promising; however, golden standard quality Monte Carlo algorithms are computationally expensive and a faster algorithm would be beneficial to adaptive proton therapy. In an ideal case, the log files would be available in real-time, and the algorithm would be fast enough to give real-time feedback. This way, the treatment plan could be interrupted while administering, decreasing the probability of complications. Unfortunately, both the log file software and the algorithms are not fast enough at this point in time.

1.3. Proton transport algorithm

Burlacu et al. [15] have developed an independent particle transport algorithm, Yet anOther Dose Algorithm (YODA), which has been proven to be faster than the proton therapy golden standard Monte Carlo algorithm [16], TOol for PArticle Simulation (TOPAS) [17]. This algorithm is based on the Linear Boltzmann Equation, where approximations are made to solve the full Linear Boltzmann Equation, which is computationally expensive to solve otherwise. These approximations result in a numerically solved partial differential equation (PDE), the Fokker-Planck equation, and an analytically solved PDE, the Fermi-Eyges equation. YODA yields the dose distribution of the inputted beamlets in a defined CT volume. This CT volume is discretized in voxels, which are small cubic volumes.

Another benefit of this algorithm is that it can use the adjoint theory. This is especially useful for daily adaptive therapy. If the plan were to be adapted daily, the input CT volume of YODA would change daily. Instead of many computationally expensive dose calculations, because there are many new repeat CT images, the adjoint method calculates an approximation of the change in dose when the treatment plan is delivered to the repeat CT scan which is computationally less expensive [16].

1.4. Research question and thesis outline

As discussed in Section 1.2, the quality assurance tool in which the delivered dose is reconstructed using log files and an independent dose algorithm and then compared planned dose is consistent with measurement-based comparisons and therefore is viable to be a faster alternative. However, often Monte Carlo-based dose calculations are used, which are computationally expensive. Burlacu et al [15] have developed an independent particle transport algorithm, YODA, which has been proven to be faster than the golden standard Monte Carlo algorithm TOPAS. The goal of the thesis is to expand and improve the existing algorithm (YODA) by calibrating YODA to the popular treatment planning software RayStation [18], while considering clinically applied range shifter components, expanding the theoretical formalism to allow realistic laterally asymmetric spot configurations and investigating the use of log files for the reconstruction of delivered doses. In doing so, the clinical applicability of this independent patient-specific QA method will be assessed by comparing the resulting dose distributions to the popular treatment planning software RayStation [18].

1.4.1. Research question

The general research question is formulated to be the following:

- How can YODA be calibrated and improved to yield dose distributions that are comparable to clinically generated dose distributions?

1.4.2. Sub-questions

This research question can be broken down into four more specific sub-questions. For each sub-question, the proposed method will be briefly discussed.

- How can YODA be calibrated to the clinically used planning software RayStation?

  The frequently used planning software RayStation outputs treatment plans in the DICOM (Digital Imaging and Communication in Medicine) format, which is the international standard format. In this format, the beamlets are defined by their nominal energy and their spot size at the isocenter in air. These treatment plans are made for the Holland PTC (HPTC) gantry. Specifically, they contain physical in-room snout to isocenter and scanning magnet to isocenter distances. YODA uses beamlet properties at the entrance of the CT image volume. Therefore, a gantry-dependent relationship between the in-air beamlet properties at the isocenter from the RayStation treatment plan and the beamlet properties at the entrance of the CT volume from the algorithm must be established. This method aims to forego matching fundamental physical data such as stopping powers, straggling coefficients, or absorption cross sections. By adjusting the inputs (mean spot energy, spot energy spread, number of protons) and lateral parameters (spot size, angular deviation, correlation) the dose distribution will be matched between the algorithms. Optimization will be used for this purpose. Here the objective is to minimize the difference between the RayStation dose distribution and the YODA dose distribution. This will be repeated with different energy spots. From this, a Beam Data Library (BDL) will be composed. This is a file that contains the nominal energy in one column and the calibrated input for YODA in the other columns.

- How can a range shifter be accounted for in YODA?

  Accounting for the range shifter in YODA can be done using a similar method to the first sub-question. Dose distributions will be generated by RayStation, now with a range shifter present. Then the beamlet parameters for YODA will be optimized to match the dose distribution of RayStation as well as possible. This will be repeated for different energy beamlets, from this again a beam data library will be composed.

- What is the error incurred in the dose distributions through the assumption of lateral spot symmetry in the solution of the Fermi-Eyges equations?

  A separability assumption has been made in the Fermi-Eyges equation resulting in two separate differential equations for x and y which are solved with identical initial conditions. To answer this subquestion, first, the Fermi-Eyges equation needs to be solved without the symmetry assumption. This is done by changing the initial conditions to be non-symmetrical. To investigate the error as a result of this assumption the difference in the integrated Fermi-Eyges flux will be calculated for symmetrical and asymmetrical cases. This difference can be directly related to the difference in dose.

- What is the effect on the dose distribution yielded by the particle transport algorithm by Burlacu et al. [15] of a systematic error in the log file beamlet parameters?

  For this part, a treatment plan will be perturbed with different systematic errors. The difference between the perturbed dose distribution and the unperturbed dose distribution will then be investigated.

When these four subquestions are investigated, the particle transport algorithm could be tested with patient log files, and the results can be compared to the planned dose distribution.

1.4.3. Thesis outline

In the next chapter, the theoretical framework of this thesis will be set. This includes an explanation of the relevant theory behind the proton transport algorithm as well as some theory on Monte Carlo-based dose calculations and the relevant theory on the model calibration. In Chapter 3, the method of this thesis will be presented. This includes the details of the calibration procedure, the methods of the performed experiments and the details of how the results of these experiments will be assessed. In Chapter 4, the results will be presented and discussed. This leads to Chapter 5, where the conclusion of this thesis will be presented along with recommendations for future research. This report has been written in the context of the Master thesis of the study Applied Physics at Delft University of Technology at the Department of Medical Physics and Technology at the Reactor Institute Delft.

2

Theory

In this chapter, the theoretical framework of this research will be set. First, the theory behind proton interactions in matter will be explained, followed by an explanation of the gantry design. Then the theory of the used dose calculation algorithms, including the mathematical framework of YODA will be explained. Lastly, the theory behind the calibration of YODA to RayStation will be explained.

2.1. Proton interactions in matter

Protons can have three distinct types of interactions with tissue: slowing down, scattering and collision with nuclei [19]. The first two are both electromagnetic interactions, whereas the last is nuclear interaction. In this section, these types of interaction will be explained.

Protons continuously lose kinetic energy due to frequent inelastic Coulomb interaction with atomic electrons [20]. The kinetic energy is not conserved, meaning the proton can transfer energy to the electrons causing the proton to slow down and the electron to ionize. An example of such an inelastic interaction is shown in Equation 2.1:

$$p + {}^{16}O \rightarrow p + {}^{16}O^{+} + e^{-}, \tag{2.1}$$

where ${}^{16}O^{+}$ denotes the ionized state of the oxygen atom. Because the proton mass is much greater than the electron mass most protons travel in a nearly straight line [20]. The rate of slowing down of the proton is dependent on the energy of the proton and the material and is called the stopping power [19].

When a proton travels close to the atomic nucleus, the proton is deflected from the straight path. This can be explained by the repulsive elastic Coulomb interaction [20]. This deflection is also referred to as scattering. Although the effect of a single scattering event is small, due to random combinations of many scatter events the total deflection on a proton beam is observable [19]. An example of elastic interaction is shown in Equation 2.2 [19]:

$$p + {}^{16}O \rightarrow p + {}^{16}O. \tag{2.2}$$

Less frequently a non-elastic nuclear reaction between protons and the atomic nucleus takes place [20]. In the non-elastic collision with the nucleus, the target nucleus, for example, may undergo breakup, be excited to a higher state or particle transfer may occur. An example of non-elastic nuclear interaction is shown in Equation 2.3 [19]:

$$p + {}^{16}O \rightarrow p + p + {}^{15}N. \tag{2.3}$$

If the proton beam is mono-energetic, all protons stop nearly at the same depth, this stopping point is referred to as the range. There is a slight spread in the range called range straggling, which is increased when the beam itself has a larger energy spread [19].

The incoming proton in an interaction is called the primary proton. With elastic interactions, the resulting proton is still the same primary proton. However, for example with non-elastic interactions, if there are two remaining protons both are called secondary as they cannot be distinguished from the primary proton [19].

Non-elastic interactions can also lead to other secondary particles, examples of possible secondaries are heavy fragments such as alpha particles, neutrons and γ rays [19]. Both the charge and the mass of these secondaries influence the particle range. For example, an alpha particle has a much shorter range than a proton, whereas a γ ray has a much longer range than a proton.

The cross-section describes the probability of proton interactions [21] and is defined by the following formula,

$$\sigma = \frac{R}{IN_a}, \tag{2.4}$$

where σ the microscopic cross section in cm^2, R is the rate of proton nuclear interactions in $\frac{\#}{cm^2 s}$, N_a is the number of target atoms per cm^2 and I is the incident beam intensity in $\frac{\#}{cm^2 s}$. This microscopic cross-section can be defined for each type of interaction separately [21]. For example, the total microscopic cross-section is the sum of the scatter and the absorption cross-sections, $\sigma_t = \sigma_s + \sigma_a$. The macroscopic cross-section can be calculated by the multiplication of the microscopic cross-section with the atomic number density, $\Sigma = N\sigma$, where N is the atomic number density in #/cm and Σ is the macroscopic cross-section in cm^{-1} [21]. This can again be done for each type of interaction separately.

2.2. Gantry design

In Figure 2.1 a schematic view of the hardware components of a gantry treatment head is displayed.

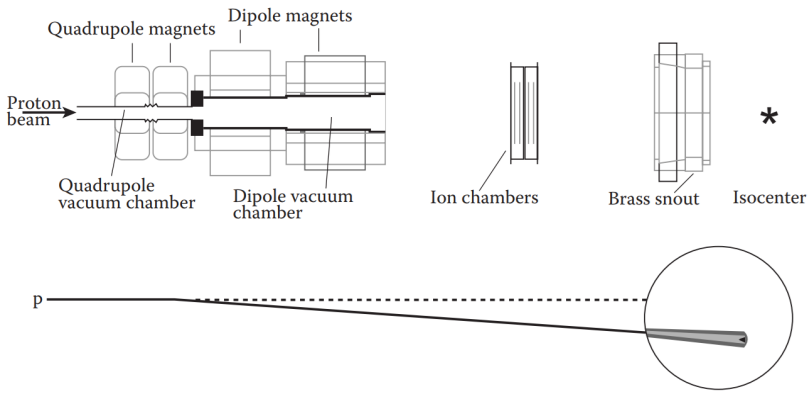

Figure 2.1: A schematic view of the hardware components of the treatment head used in pencil beam scanning, including the deflection of the pencil beam. Adapted from Paganetti [19].

The size of the proton beam coming from the accelerator is adjusted by the quadrupole magnets shown in Figure 2.1 [19]. In modern proton therapy, pencil beam scanning (PBS) is used to irradiate the tumor volume. Dipole magnets or scanning magnets, as shown in Figure 2.1, are used to laterally cover the intended area with narrow proton beams while energy modulation covers the depth [5]. These beams are called pencil beams, beamlets or spots. Figure 2.1 shows the deflection of a single pencil beam steered by the dipole magnets. Beam scanning allows for intensity modulated proton therapy (IMPT), where the spot position, energy and fluence are optimized independently for each spot [5]. The ion chamber, shown in Figure 2.1, is used to measure the dose, position and beam profiles before the beam exits through the snout of the treatment head [19]. Both the gantry and the treatment couch on which the patient is positioned can rotate, as shown in Figure 2.2. This combination of gantry angle and couch angle leads to good coverage of the patient. Isocenter is defined as the point where the central beam axes for any gantry angle coincide [19]. The depth of the tumor dictates the needed beam energy, with shallower tumors requiring lower beam energies.

Due to accelerator design limitations, range shifters (RS) are used to slow down the proton beam beyond the minimum obtainable accelerator beam energy [19]. A range shifter is a slab of material, which can be produced in varying widths depending on the desired range, that is placed in the beam path to slow down protons. Due to the elastic Coulomb interaction within the range shifter, the proton energy decreases, resulting in a shallower range, while the inelastic Coulomb interaction causes the protons to scatter resulting in a bigger spot size [19].

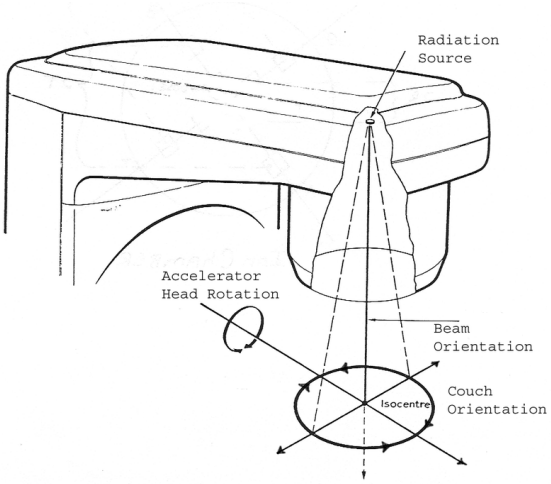

Figure 2.2: Schematic view of the gantry and couch rotation. Adapted from Romeijn [22]

The angular spread of the beam and the energy spread are increased as well [19]. Both the material and the thickness influence the amount of energy that is dissipated in the range shifter as a result of proton interaction with the slab. Often range shifter materials are types of plastic, as the scattering is lower per unit of range shift compared to other materials [19]. The exact material used in treatment is chosen based on the desired effect of the range shifter and its known properties such as density and stopping power. Also, other factors such as cost, material uniformity and rigidness should be taken into consideration [23]. Using a range shifter results in a shallower range, which is convenient when dealing with shallow-placed target volumes [19], while the number of spots needed to irradiate a volume decreases due to the increase in spot size. The broadening of the spot can be reduced by reducing the air gap between the range shifter and the patient [23]. The exact position of the range shifter in the treatment head can slightly differ per treatment system, it can be placed before the ion chamber, shown in Figure 2.1, as the proton beam range is then modified before the measurement. It is often placed near the end of the treatment head to reduce the air gap between the range shifter and the patient.

2.3. Dose calculation algorithms

In this thesis, the deterministic dose algorithm, YODA, will be calibrated to the Monte Carlo-based planning system, RayStation. In this section, the mathematical framework of YODA will be explained followed by an explanation of the general workings of Monte Carlo dose algorithms.

2.3.1. Deterministic dose algorithm

YODA is a deterministic proton transport algorithm that uses the steady-state Linear Boltzmann Equation (LBE) as a foundation. This can be rewritten into two partial differential equations (PDE), the Fermi-Eyges (FE) and the Fokker-Planck (FP) equation. Leading to two solutions that, when combined, can provide the deposited energy in a volume. Only the main details of the derivation published by Burlacu et al. [15] will be explained in this section.

2.3.1.1. Steady state linear Boltzmann equation

The LBE is an equation that describes the proton balance in an arbitrary volume [15]. Burlacu et al. [15] describe that this is done by accounting for all proton loss and gain mechanisms in an arbitrary volume V for protons with position $\boldsymbol{r} \in \mathbb{R}^3$, energy E and direction $\hat{\boldsymbol{\Omega}} = \mathrm{v}/|\mathrm{v}|$, where v is the velocity vector of the protons, following Duderstadt and Hamilton [21]. The steady-state LBE is defined by Burlacu et al. [15] to be,

$$\hat{\boldsymbol{\Omega}} \cdot \nabla\phi + \Sigma_t(\boldsymbol{r}, E)\phi(\boldsymbol{r}, E, \hat{\boldsymbol{\Omega}}) = \int_{4\pi} \mathrm{d}\hat{\boldsymbol{\Omega}}' \int_0^\infty \mathrm{d}E' \Sigma_s(E' \to E, \hat{\boldsymbol{\Omega}}' \to \hat{\boldsymbol{\Omega}})\phi(\boldsymbol{r}, E', \hat{\boldsymbol{\Omega}}') + s(\boldsymbol{r}, E, \hat{\boldsymbol{\Omega}}) \tag{2.5}$$

$$BC : \phi(\boldsymbol{r}_s, E, \hat{\boldsymbol{\Omega}}) = 0 \text{ if } \hat{\boldsymbol{\Omega}} \cdot \hat{\boldsymbol{e}}_s < 0 \text{ with } \boldsymbol{r}_s \in \partial V, \tag{2.6}$$

where $\phi = vn$ describes the proton flux with v is the proton speed and $n(\boldsymbol{r}, E, \hat{\boldsymbol{\Omega}})$ is the angular proton density. BC is the boundary condition, $\boldsymbol{r}_s$ describes a vector on the boundary surface ∂V, $\hat{\boldsymbol{e}}_s$ is the unit outward pointing

normal vector to the boundary ∂V at $\boldsymbol{r}_s$, Σ_t is the total macroscopic cross section, Σ_s is the macroscopic double differential scattering cross section where s describes the source of the protons.

The total cross-section can be written as $\Sigma_t = \Sigma_a + \Sigma_e + \Sigma_{in}$ where Σ_a is the catastrophic absorption scatter cross-section, Σ_e is the elastic scatter cross-section between incident protons and the nuclei of the tissue and Σ_{in} is the inelastic scatter cross-section between the incident protons and atomic electrons. Doing the same for Σ_s transforms equation 2.5 into [15]

$$\begin{aligned}\hat{\boldsymbol{\Omega}}\cdot\nabla\phi = &\int_{4\pi} \mathrm{d}\hat{\boldsymbol{\Omega}}' \int_E^\infty \mathrm{d}E'\Sigma_a(E'\rightarrow E, \hat{\boldsymbol{\Omega}}'\rightarrow\hat{\boldsymbol{\Omega}})\phi(\boldsymbol{r},E',\hat{\boldsymbol{\Omega}}') - \Sigma_a(\boldsymbol{r},E)\phi(\boldsymbol{r},E,\hat{\boldsymbol{\Omega}}) \\ &+ \int_{4\pi} \mathrm{d}\hat{\boldsymbol{\Omega}}'\Sigma_e(\boldsymbol{r},E,\hat{\boldsymbol{\Omega}}'\rightarrow\hat{\boldsymbol{\Omega}})\phi(\boldsymbol{r},E,\hat{\boldsymbol{\Omega}}') - \Sigma_e(\boldsymbol{r},E)\phi(\boldsymbol{r},E,\hat{\boldsymbol{\Omega}}) \\ &+ \int_0^\infty \mathrm{d}Q\Sigma_{in}(\boldsymbol{r},E+Q\rightarrow E,\hat{\boldsymbol{\Omega}})\phi(\boldsymbol{r},E+Q,\hat{\boldsymbol{\Omega}}) - \Sigma_{in}(\boldsymbol{r},E)\phi(\boldsymbol{r},E,\hat{\boldsymbol{\Omega}}),\end{aligned} \tag{2.7}$$

where Q is the amount of energy transferred during an interaction. The energy transfer in Coulomb elastic scatter interactions and the angular deflection in Coulomb inelastic scatter interactions are neglected.

To further simplify Equation 2.7, the Continuous Slowing Down Approximation (CSDA) and the Energy-Loss Straggling (ELS) approximation are applied [15]. Due to the difference in proton and electron mass, the energy loss of the proton in a collision is small. The stopping of the proton beam can be approximated by continuously losing energy. The mean will be called the stopping power and the deviation around the mean will be called the straggling coefficient.

The small angle Fokker-Planck approximation is applied on the elastic scatter angular integral while orienting the beam along the z-direction, here $\hat{\boldsymbol{\Omega}} = (\Omega_x, \Omega_y) \in \mathbb{R}^2$ [15]. Due to the small angular deflection caused by Coulomb interactions with the atom, the scattering process can be approximated as a continuous diffusion term in the lateral angular plane averaged over the energy spectrum, $\overline{\Sigma_{tr}}(z)$ [16].

The application of these approximations leads to the following PDE [15]

$$\frac{\partial\phi}{\partial z} + \Omega_x\frac{\partial\phi}{\partial x} + \Omega_y\frac{\partial\phi}{\partial y} - \frac{\partial S(\boldsymbol{r},E)\phi}{\partial E} - \frac{1}{2}\frac{\partial^2 T(\boldsymbol{r},E)\phi}{\partial E^2} + \Sigma_a(\boldsymbol{r},E)\phi - \overline{\Sigma_{tr}}(z)\left(\frac{\partial^2\phi}{\partial\Omega_x^2} + \frac{\partial^2\phi}{\partial\Omega_y^2}\right) = 0, \tag{2.8}$$

where $S(\boldsymbol{r},E)$ describes the stopping power, $T(\boldsymbol{r},E)$ describes the straggling coefficient. $\Sigma_a(\boldsymbol{r},E)$ is the absorption cross section, and $\overline{\Sigma_{tr}}(z)$ is the energy spectrum averaged transport cross section. The proton flux ϕ is dependent on $\boldsymbol{r}, \hat{\boldsymbol{\Omega}}$ and E. However, this notation was dropped for readability. By applying energy separability, the flux is written as [15]

$$\phi = \phi_{FE}(\boldsymbol{r},\hat{\boldsymbol{\Omega}})\cdot\phi_{FP}(z,E), \tag{2.9}$$

while considering a laterally homogeneous, in-depth heterogeneous geometry. To further simplify the notation the dependence of $\phi_{FE}(\boldsymbol{r},\hat{\boldsymbol{\Omega}})$ and $\phi_{FP}(z,E)$ on $(\boldsymbol{r},\hat{\boldsymbol{\Omega}})$ and (z,E) will from now on be dropped. Equation 2.8 can now be written as

$$\Upsilon(\phi_{FE})\cdot\phi_{FP} + \phi_{FE}\cdot 1DFP(\phi_{FP}) = 0, \tag{2.10}$$

where $\Upsilon(\phi_{FE})$ is the Fermi-Eyges equation and $1DFP(\phi_{FP})$ is the one dimensional Fokker-Planck equation. Both equations are set to zero using separation of variables [15].

$$\Upsilon(\phi_{FE}) = \frac{\partial\phi_{FE}}{\partial z} + \Omega_x\frac{\partial\phi_{FE}}{\partial x} + \Omega_y\frac{\partial\phi_{FE}}{\partial y} - \overline{\Sigma_{tr}}(z)\left(\frac{\partial^2\phi_{FE}}{\partial\Omega_x^2} + \frac{\partial^2\phi_{FE}}{\partial\Omega_y^2}\right) = 0 \tag{2.11}$$

$$1DFP(\phi_{FP}) = \frac{\partial\phi_{FP}}{\partial z} - \frac{\partial S(z,E)\phi_{FP}}{\partial E} - \frac{1}{2}\frac{\partial^2 T(z,E)\phi_{FP}}{\partial E^2} + \Sigma_a(z,E)\phi_{FP} = 0 \tag{2.12}$$

2.3.1.2. Fermi-Eyges equation

According to Gebäck and Asadzadeh [24], the Fermi-Eyges equation, as shown in Equation 2.11, can be solved analytically. The equation is separated in the x and y directions, $\phi_{FE}(\boldsymbol{r},\Omega_x,\Omega_y) = H(z,x,\Omega_x)\cdot H(z,y,\Omega_y)$ resulting in the following equation

$$\frac{\partial H(z,\xi,\omega)}{\partial z} + \omega\frac{\partial H(z,\xi,\omega)}{\partial \xi} - \overline{\Sigma_{tr}}(z)\frac{\partial^2 H(z,\xi,\omega)}{\partial \omega^2} = 0, \tag{2.13}$$

where ξ can be either x or y and ω can be Ω_x or Ω_y. The same boundary condition is imposed on both PDEs,

$$H(0,\xi,\omega) = Cexp(-(a_1\xi^2 + a_2\xi\omega + a_3\omega^2)), \tag{2.14}$$

where $a_i \in \mathbb{R}, \forall i = [1,2,3]$ and $C > 0$.

The solution can be found by extending the domain of Ω_x and Ω_y to $(\Omega_x,\Omega_y) \in [-\infty,\infty]^2$ and applying two-dimensional Fourier transforms in ξ and ω and solving for the Gaussian initial condition [15]. The solution is found to be [24]

$$\phi_{FE}(z,\boldsymbol{\rho},\hat{\boldsymbol{\Omega}}) = \frac{A^2}{4\pi^2}\frac{\exp\left(-\frac{|\boldsymbol{\rho}|^2}{2\overline{\xi^2}(z)}\right)}{\overline{\xi^2}(z)}\frac{\exp\left(-\frac{1}{2B(z)}\left|\hat{\boldsymbol{\Omega}} - \frac{\overline{\Theta\xi}(z)}{\overline{\xi^2}(z)}\boldsymbol{\rho}\right|^2\right)}{B(z)}, \tag{2.15}$$

where $\boldsymbol{\rho} = (x,y)$, $\hat{\boldsymbol{\Omega}} = (\Omega_x,\Omega_y)$ and $B(z) = \overline{\Theta^2}(z) - \frac{(\overline{\Theta\xi}(z))^2}{\overline{\xi^2}(z)}$, $A = \frac{2\pi C}{D}$, $D = 4a_1a_3 - a_2^2$. The coefficients $\overline{\Theta^2},\overline{\Theta\xi},\overline{\xi^2}$ can be found using the following equations,

$$\overline{\Theta^2}(z) = \overline{\Theta^2}(0) + \int_0^z \overline{\Sigma_{tr}}(z')\mathrm{d}z', \quad \text{with} \quad \overline{\Theta^2}(0) = \frac{2a_1}{D}, \tag{2.16}$$

$$\overline{\Theta\xi}(z) = \overline{\Theta\xi}(0) + \overline{\Theta^2}(0)z + \int_0^z (z-z')\overline{\Sigma_{tr}}(z')\mathrm{d}z', \quad \text{with} \quad \overline{\Theta\xi}(0) = \frac{-a_2}{D}, \tag{2.17}$$

$$\overline{\xi^2}(z) = \overline{\xi^2}(0) + 2\overline{\Theta\xi}(0)z + \overline{\Theta^2}(0)z^2 + \int_0^z (z-z')^2\overline{\Sigma_{tr}}(z')\mathrm{d}z', \quad \text{with} \quad \overline{\xi^2}(0) = \frac{2a_3}{D}, \tag{2.18}$$

and

$$\overline{\Sigma_{tr}}(z) = \int \mathrm{d}E\phi_{FP}(z,E)\Sigma_{tr}(z,E)\Big/\int \mathrm{d}E\phi_{FP}(z,E), \tag{2.19}$$

where

$$\Sigma_{tr}(z,E) = \int_{-1}^{1}\mathrm{d}\mu\Sigma_s(E,\mu,z)(1-\mu), \text{ with } \mu = \cos\left(\hat{\boldsymbol{\Omega}},\hat{\boldsymbol{\Omega}}'\right), \tag{2.20}$$

and Σ_s is the macroscopic elastic scatter cross-section. Note that the coefficients $\overline{\Theta^2}(0) = \frac{2a_1}{D}$, $\overline{\Theta\xi}(0) = \frac{-a_2}{D}$ and $\overline{\xi^2}(0) = \frac{2a_3}{D}$ differ from what was published by Gebäck and Asadzadeh [24]. The derivation shown in Appendix A, shows that the original paper by Gebäck and Asadzadeh [24] likely contained a typo. The coefficients of the boundary condition are chosen to be a two-dimensional normal distribution [15]. When setting the average values of ξ and ω to zero $a_i, i \in [1,2,3]$ are described by

$$a_1 = \frac{1}{2(1-\varrho^2)\sigma_\xi^2}, \quad a_2 = -\frac{\varrho}{(1-\varrho^2)\sigma_\xi\sigma_\omega}, \quad a_3 = \frac{1}{2(1-\varrho^2)\sigma_\omega^2}, \tag{2.21}$$

where ϱ the correlation coefficient between the spatial dimension ξ, the angular dimension ω, σ_ξ is the standard deviation in ξ and σ_ω is the standard deviation in ω.

2.3.1.3. Fokker-Planck equation

The Fokker-Planck equation, as shown in Equation 2.12, can be solved numerically by using the Symmetric Interior Penalty Galerkin (SIPG) method in the energy domain and the Singly Diagonally Implicit Runge-Kutta (SDIRK) method in space [16].

The one-dimensional Fokker-Planck equation has the following boundary conditions in energy (BCE) and space (BCS) [16],

$$BCE: \phi_{FP}(z,E)\Big|_{E=E_{max}} = 0, \quad \frac{\partial \phi_{FP}(z,E)}{\partial E}\Big|_{E=E_{max}} = 0, \quad \frac{\partial \phi_{FP}(z,E)}{\partial E}\Big|_{E=E_{min}} = 0, \tag{2.22}$$

$$BCS: \phi_{FP}(0,E) = Ae^{-\left(\frac{E-E_0}{\sigma_E}\right)^2}, \tag{2.23}$$

where BCS is a Gaussian function with amplitude A, nominal beam energy E_0 and σ_E is the energy spread.

The energy domain is discretized in NG intervals referred to as energy groups that have the same width, ranging from E_{min} to E_{max} [15]. Where the energy domain is chosen to be the clinical proton energy range of 1 MeV to 200 MeV. The boundaries of an energy group are $E_{g+1/2}$ and $E_{g-1/2}$, the center value is E_g. Thus $E_{min} = E_{NG+1/2}$ and $E_{max} = E_{1/2}$. A schematic view of this energy discretization is provided in Figure 2.3.

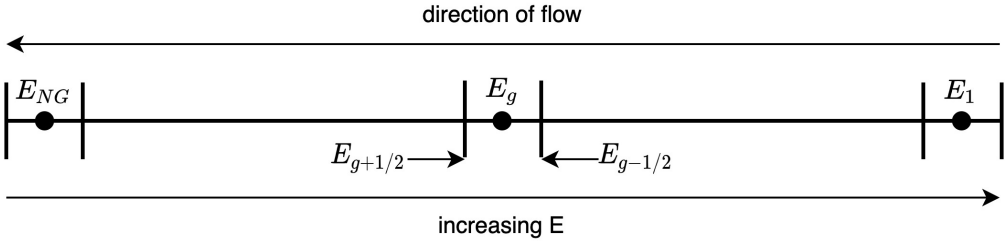

Figure 2.3: A schematic view of the energy discretization used in YODA. Adapted from Burlacu et al. [15].

The spatial domain is discretized in N_s steps with length Δz which is allowed to vary per step. The starting point is $z_0 = 0$ and $z_{Ns} = z_{max}$ [15].

The Equation 2.12 can then be rewritten to be a system of equations which can be solved using an off-the-shelf banded system solver [15].

2.3.1.4. Deposited energy

The CT image volume is given by the union of all its N_v voxels ($k = 1, ..., N_v$, where V_k is the volume of one voxel) [16]. The Fokker-Planck and Fermi-Eyges solutions can be used to obtain the deposited energy in the CT volume. Let, Ψ_{FE} be the angular integtral of ϕ_{FE} [16], also referred to as the integrated Fermi-Eyges flux,

$$\Psi_{FE}(\boldsymbol{r}) = \int_{4\pi} \mathrm{d}\hat{\boldsymbol{\Omega}} \phi_{FE}(\boldsymbol{r}, \hat{\boldsymbol{\Omega}}) = \frac{A^2}{2\pi\overline{\xi^2}(z)} \exp\left(-\frac{x^2+y^2}{2\overline{\xi^2}(z)}\right), \tag{2.24}$$

and let Ψ_{FP} be defined as

$$\Psi_{FP}(z) = \int_0^\infty \mathrm{d}E E\left[-\frac{\partial S(z,E)\phi_{FP}}{\partial E} - \frac{1}{2}\frac{\partial^2 T(z,E)\phi_{FP}}{\partial E^2} + \Sigma_a(z,E)\phi_{FP}\right]. \tag{2.25}$$

Combining the Ψ_{FE} and Ψ_{FP} the energy deposited in a voxel V_k is given by the following equation [16]

$$E_k = \int_{V_k} \mathrm{d}V \Psi_{FE}(\boldsymbol{r}) \Psi_{FP}(z). \tag{2.26}$$

From this, the delivered dose to the voxel V_k can be calculated using [16]

$$D_k = \frac{E_k}{m_k} = \frac{1}{\Delta V} \int_{V_k} \mathrm{d}V \frac{\Psi_{FE}(\boldsymbol{r}) \Psi_{FP}(z)}{\rho_k}, \tag{2.27}$$

where m_k is the mass of a voxel V_k, $\Delta V = \Delta x \Delta y \Delta z$ is the volume of a voxel V_k and ρ_k is the mass density of a voxel V_k.

The energy or dose deposited in the entire CT volume can be found by summing Equations 2.26 and 2.27, respectively, over all k in the CT volume.

2.3.2. Monte Carlo dose algorithm

As ground truth, in the calibration procedure, dose calculations from RayStation will be used. RayStation is a Monte Carlo-based treatment planning system (TPS). In this section, the general workings of a Monte Carlo dose algorithm will be discussed.

Monte Carlo algorithms sample following stochastic probability distributions and are based on the central limit theorem [19]. In proton transport, this probability distribution describes every possible physical interaction and its outcome. This is repeated for every step in the defined geometry, the CT volume.

A particle's history is defined as the trajectory of a particle and all its possible secondaries [19]. A simulation of a particle history starts with sampling from a starting source distribution. Then one particle at a time and one step at a time, the particle will be tracked through the geometry sampling from different distributions to determine how the particle might interact.

The outcome of a Monte Carlo algorithm is heavily based on the number of particles and the step size [19]. To achieve high accuracy it is best to use many particles and small step sizes. However, when taking small step sizes the calculation can become computationally expensive. One proposed way to lessen this computational load by Paganetti [19] is to reduce coulomb scattering to one step, where multiple scattering theories provide a probability distribution for the total angle after one step. Paganetti [19] suggest that one can also choose not to track every single secondary. But when Monte Carlo algorithms are used as the golden standard, they should aim to be a complete simulation of all interactions with matter [25].

2.4. Model calibration

In this section, the relevant theory for the model calibration will be discussed. First, the parameters that need to be calibrated will be presented. Then, the theory behind the optimization method that will be used for the calibration will be discussed. Lastly, the equation to determine the agreement between reference and calibrated data, the gamma index, will be explained.

2.4.1. Beamlet parameters

The treatment plans are outputted in DICOM format by RayStation. In this format, the beamlets are defined by their nominal energy and their spot size at the isocenter in the air and these plans are gantry-specific, as they contain the snout to isocenter distance. YODA however, uses the beamlet properties defined at the entrance of the CT volume. To be able to compare YODA doses with RayStation doses, the beamlet parameters need to be calibrated by establishing a gantry-dependent relationship between the in-air beamlet properties at the isocenter from the Raystation treatment plan and the beamlet properties at the entrance of the CT volume for YODA. The beamlet parameters inputted to YODA include the following: position of the spot, spot mean energy E in MeV, energy spread σ_E in MeV, number of protons NP, spatial spread σ_x in cm, angular spread σ_{Ω_x} in radians and the correlation ϱ between the spatial and angular dimensions. Furthermore, the CT volume is also inputted to YODA. The RayStation DICOM RT plan provides the spot position, the planned spot energy and the monitoring units (MU) for a plan specified in a certain CT volume. The MU is a quantity that describes the charge collected in the transmission ion chamber in the treatment head needed to provide the prescribed dose [19].

When calibrating, the same CT volume and spot positions will be used for both the RayStation reference dose distribution and the YODA dose distribution. This leaves the following parameters to be calibrated: the spot mean energy, energy spread, number of protons, spatial spread, angular spread and correlation between the spatial and angular dimensions.

Note that the number of protons retrieved from the calibration is specific for the MU specified in the treatment plan provided by RayStation that was used for the calibration. To generalize the results for other treatment plans the number of protons per MU should be calculated and stored.

2.4.2. Trust region optimization

In this thesis, an optimization technique called trust region optimization will be used to calibrate YODA to RayStation. This technique was chosen as it does not necessarily require the gradient of the function that is to be optimized and the step size is variable per iteration, making fast convergence possible. First, an objective function is defined, which is the function that will be minimized. Then a starting point is provided to the

algorithm which is the best-known solution to the objective. It starts by approximating a region around the best-known solution of the objective using a model, which is often a quadratic model, of the objective function [26]. A neighborhood around the best-known solution in this model is created using a trust radius, this is called the trust region, as this should be a fair approximation of the actual objective function. Then, the minimal solution in this trust region to the model is found. This point is taken as the new best-known solution to the actual objective function and the value is calculated. This is an iterative process that will be repeated until the solution satisfies the stopping conditions. The size of the trust region is dependent on the previous step [27]. If the previous step approximated the function well, the trust radius can be enlarged for the next step. However, if the last iteration was a bad approximation, the trust radius will be decreased for the next iteration. Trust region optimisation can be applied to problems with multiple optimization parameters and this method is also compatible with bounds and constraints [28] as there can not be a trust region at points where the bounds and constraints are not met.

2.4.3. Gamma index

The gamma index is a clinically used quantity that gives insight into the difference between a reference dose distribution and a dose distribution that is to be evaluated. Low et al. [29] gives the following set of equations,

$$\Gamma(\boldsymbol{r}_e, \boldsymbol{r}_r) = \sqrt{\frac{\delta^2(\boldsymbol{r}_e, \boldsymbol{r}_r)}{\Delta D^2} + \frac{r^2(\boldsymbol{r}_e, \boldsymbol{r}_r)}{\Delta d^2}}, \tag{2.28}$$

where

$$\delta(\boldsymbol{r}_e, \boldsymbol{r}_r) = D_e(\boldsymbol{r}_e) - D_r(\boldsymbol{r}_r), \tag{2.29}$$

and

$$r(\boldsymbol{r}_e, \boldsymbol{r}_r) = |\boldsymbol{r}_e - \boldsymbol{r}_r|, \tag{2.30}$$

where $\boldsymbol{r}_e$ describes a position in the evaluation dose distribution, $\boldsymbol{r}_r$ describes a position in the reference dose distribution and where $D_e(\boldsymbol{r}_e)$ describes the dose at $\boldsymbol{r}_e$ of the evaluation dose distribution and $D_r(\boldsymbol{r}_r)$ describes the dose at $\boldsymbol{r}_r$ of the reference dose distribution. ΔD is the dose difference criterion and Δd is the distance to agreement (DTA) criterion. The gamma index then can be found by,

$$\gamma(\boldsymbol{r}_r) = \min\{\Gamma(\boldsymbol{r}_e, \boldsymbol{r}_r)\} \forall \{\boldsymbol{r}_e\}, \tag{2.31}$$

Low et al. [29] then introduced a pass-fail criterion which states that when $\gamma \leq 1$ the calculation passes. The differences between the two dose distributions are then acceptable for clinical practice.

This calculation can be visualized by an ellipsoid in a space defined on one axis by dose and on the other by distance [29]. The ellipsoid's size is determined by the acceptance criteria and is centered around the reference dose point. If the evaluated dose point falls within or on the surface of this ellipsoid the calculation is accepted. The evaluated dose point closest to the center of the ellipsoid will be used to calculate the gamma index. This is shown in Figure 2.4. Note that in this figure the δ axis describes the dose, the x axis the distance, the subscript 'c' refers to the evaluation dose distribution and subscript 'm' refers to the reference dose distribution.

Using this gamma index, a passing rate can be calculated for the whole dose distribution, by simply calculating the percentage of gamma indexes equal to or smaller than 1 in the evaluation dose distribution.

Das et al. [30] state that for photon therapy often $\Delta d = 3$ mm and $\Delta D = 3\%$ are used and a passing rate of 90% is followed by many institutions. By lowering Δd and ΔD, to for example 1 mm and 1% the acceptance criteria will be stricter, and the dose distributions then need to be more similar to pass.

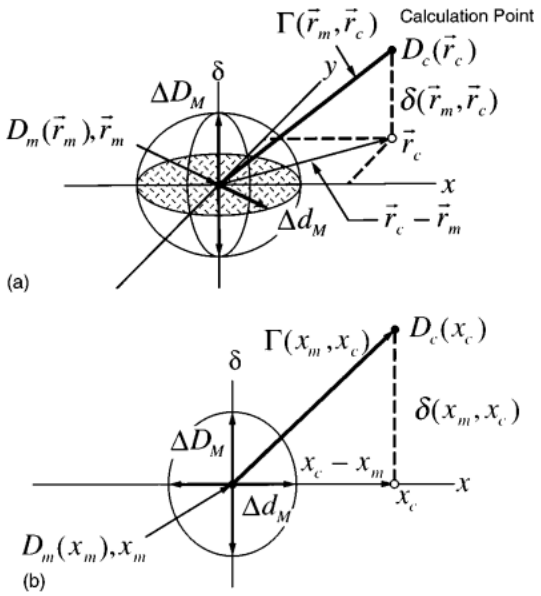

Figure 2.4: Geometric representation of dose distribution evaluation criteria using the combined ellipsoidal dose-difference and distance-to-agreement tests. (a) Two-dimensional representation. (b) One-dimensional representation. Adapted from Low et al. [29]. Note that the subscript 'c' refers to the evaluation dose distribution and subscript 'm' refers to the reference dose distribution.

3

Methods

In this chapter, the method that was used during this thesis will be explained. Firstly, the details of the calibration procedure will be discussed. Secondly, the methods used to perform the experiments will be explained, and lastly, the metrics used to compare the results to their corresponding reference dose will be listed.

3.1. Calibration procedure

To calibrate YODA to RayStation an optimization procedure was used. In this section, this procedure will be discussed. To optimize, a water box of 100 mm by 300 mm by 100 mm was used as the CT volume in which a single spot was irradiated from a 0° gantry angle. This means that the central beam axis is along the y direction and the x,z plane is the lateral plane.

3.1.1. Beam data library

This thesis aims to adapt the already existing deterministic dose algorithm to use it for patient-specific QA by comparing planned dose and reconstructed delivered dose. To compare the planned dose to the reconstructed dose, computed by an independent proton algorithm, the input parameters need to be calibrated. For this purpose, a beam data library (BDL) can be used, which is a file where parameters are stored that characterize a spot for different energies [31]. This file will, in this case, be used as a calibration table between RayStation and YODA, as the file describes the parameters needed in YODA to reproduce a spot planned by RayStation. This file contains both the nominal spot energy planned by RayStation and the mean spot energy found for YODA along with the energy spread, number of protons per MU, spatial spread, angular spread and the correlation between the spatial and angular dimensions. The file also contains information on the presence of a possible range shifter. The calibration was performed for several different planned spot energies however, when the desired planned energy for a dose comparison is not present in the BDL, linear interpolation can be used to obtain the beamlet parameters for YODA.

3.1.2. Objective function

The objective function was chosen to be the squared difference of the dose distributions summed for all voxels in the CT volume. For the spots planned without range shifters it is defined to be the following,

$$J(\alpha) = \sum_{k=1}^{N_v} (D_Y(V_k, \alpha) - D_R(V_k))^2, \tag{3.1}$$

where $D_Y(V_k, \alpha)$ is the dose deposited in the voxel V_k found in the dose distribution yielded by YODA, $D_R(V_k)$ is the dose deposited in the voxel V_k found in the provided RayStation planned dose distribution, N_v is the number of voxels and α is a vector containing the input beamlet parameters that are to be optimized.

When calibrating for spots that include range shifters, a weight was used over both the dose distributions in the objective function. This weight was a 2D Gaussian function in the lateral plane. The spread is extracted from a fit of the lateral profile of the beamlet at the Bragg peak from the RayStation dose distribution. Extra weights were added in depth around the Bragg peak, a factor of 2 for the 5 layers of voxels before and after the

Bragg peak, leading to the following objective,

$$J(\alpha) = \sum_{k=1}^{N_v} (W(V_k)(D_Y(V_k,\alpha) - D_R(V_k))^2), \tag{3.2}$$

where $W(V_k)$ is the value of the weight matrix in voxel V_k.

3.1.3. Approximation to improve inclusion of nuclear interactions

In the early stages of testing the optimization procedure, it was suspected that the nuclear interactions needed to be modelled in a different way to improve the results. In YODA, all of the energy of the secondaries due to nuclear interaction was deposited locally. This is a crude assumption and therefore an alternative was introduced. Bortfeld [32] suggested depositing a percentage locally and neglecting the rest of the energy, as not all secondaries have a short range. An alpha particle has a short range, therefore, locally depositing the dose of this alpha particle as a result of nuclear interaction can be justified. However, a photon or a neutron has a much longer range, the particle will likely exit the patient's body, and therefore the dose will not be deposited in the volume. In this case, it could not be justified to deposit the dose locally as a result of these secondaries. Bortfeld [32] reported reasonable results despite the crudeness of the suggested method. The percentage of locally deposited dose suggested in the paper was around 60%.

In this thesis, this idea was used, but with some alterations. The percentage of the locally deposited dose was included in deposited energy, Equation 2.26, by introducing it in $\Psi_{FP}(z)$ as described in Equation 2.25, leading to the following equation:

$$\Psi_{FP}(z) = \int_0^\infty \mathrm{d}EE \left[-\frac{\partial S(z,E)\phi_{FP}}{\partial E} - \frac{1}{2}\frac{\partial^2 T(z,E)\phi_{FP}}{\partial^2 E} + \gamma \Sigma_a(z,E)\phi_{FP} \right], \tag{3.3}$$

where γ represents the percentage of locally deposited dose due to nuclear interactions.

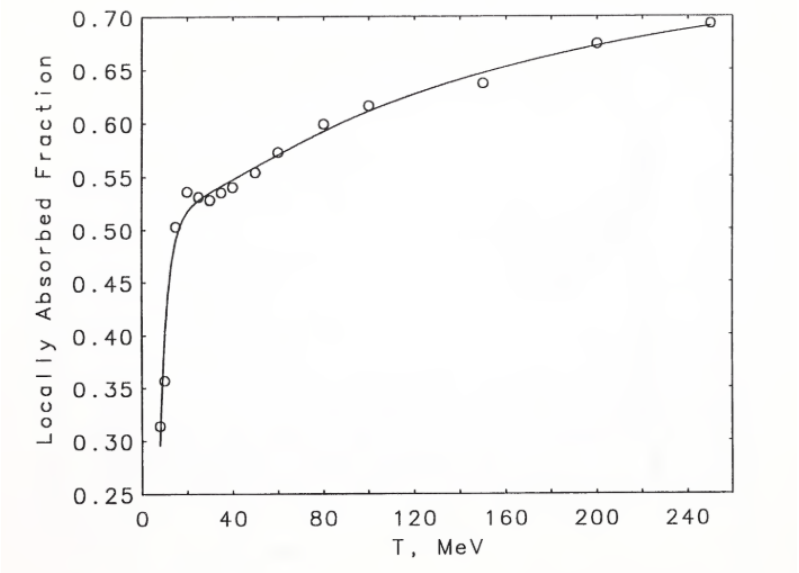

Figure 3.1: Fraction of the energy lost by a proton in a nonelastic nuclear reaction that is transferred to secondary charged particles (Seltzer, 1992 [33]). The points represent the calculations, and the curve is a least-squares fit. Adapted from Berger [34] .

Figure 3.1 shows the fraction of the energy lost by a proton in a nonelastic nuclear reaction that is transferred to secondary charged particles as presented by Berger [34]. This figure suggests that there should be a decreasing dependency between the beam energy and γ, as the proton loses less energy to secondaries for lower beam energies. Therefore, γ was optimized at different mean beam energies and a constraint was imposed on the optimization that γ should be decreasing with decreasing energy. The energy points at which γ was optimized were at 100%, 90%, 80%, 70%, 60%, 50%, 40%, 20% and 0% of the mean beam energy relative to the initial mean beam energy. In between these energies, the value of γ was found by using linear interpolation between

the optimized γ points. This adds 9 additional optimization parameters. Because γ is a fraction, its value is bounded between 0 and 1. The optimized values of this γ are then also stored in the BDL.

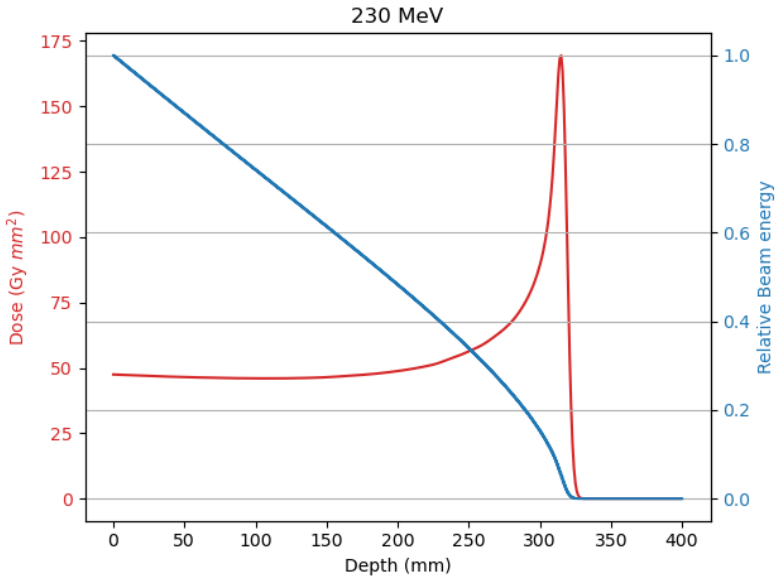

Figure 3.2: The integral depth dose curve (in red) of a 230 MeV spot and the relative beam energy (in blue) plotted against the depth displayed in the same figure.

The choice was made to use more points in the high-energy domain and fewer in the low-energy domain, as the effect of the varying γ was smaller in the low-energy parts, occurring after the Bragg peak. Figure 3.2 shows the Integral Depth Dose curve (IDD) and the relative beam energy against the depth of a single spot with 230 MeV beam energy. The IDD is defined as the sum of the dose distribution over the lateral plane as a function of depth, $\mathrm{IDD}(z) = \int\int_{X,Y} D(x,y,z)\mathrm{d}x\mathrm{d}y$, where z is the depth. The energy points at which γ was optimized cover the IDD curve reasonably as the mean beam energy decreases to zero just after the Bragg peak as can be seen in Figure 3.2.

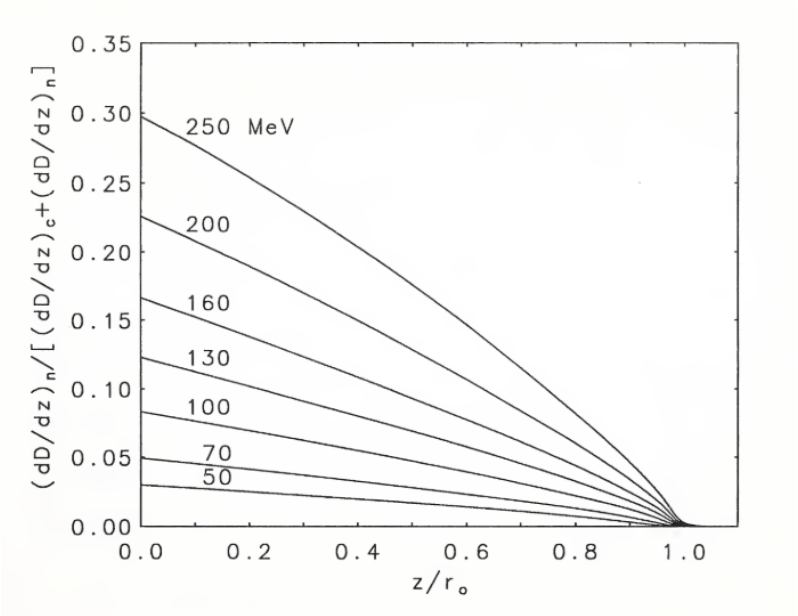

Figure 3.3: Fraction of the absorbed dose that is contributed by secondary charged particles from nuclear reactions. Adapted from Berger [34]. Where the x-axis shows the depth normalized with the range of the beam.

Figure 3.3 shows the relation between the fraction of absorbed dose due to secondaries resulting from nuclear

interactions against depth normalized with range for different initial beam energies as published by Berger [34]. This suggests that there is a difference in the dose that needs to be locally deposited for different initial beam energies. Therefore, γ was optimized for every initial beam energy.

3.1.4. Optimization variables and bounds

The optimization parameters consist of the system parameters discussed in Section 2.4.1 and the γ introduced in Section 3.1.3: the mean spot energy E in MeV, the energy spread σ_E in MeV, the number of protons NP, the spatial spread σ_x in cm, the angular spread σ_{Ω_x} in radians, the correlation between the spatial and angular dimension ϱ and the fraction of locally deposited dose γ. These characterize the beamlet and therefore need to be optimized against RayStation.

To set the bounds, an already available BDL was used for spots without a range shifter. This BDL was made specifically for the Monte Carlo dose engine MC^2 and measurements performed at HPTC. This BDL can provide an idea as to what the order of magnitude is that the parameters should be in. It cannot provide an accurate result as it is specifically made for the HPTC gantry in combination with MC^2 and not for YODA. However, the HPTC BDL was used to provide an initial guess for the minimization function as again, it should be in the right order of magnitude. YODA assumes that a spot is symmetric in the lateral plane, while in the HPTC BDL, the spatial spread, angular spread and correlation for both the x and y directions were provided. YODA takes the mean of these parameters and uses that for the symmetrical spot. For the number of protons, the initial guess was found by using the relation for dose and energy in a voxel V_k, $D_k = E_k/m_k$. By multiplying the total dose by the mass of the volume and dividing by the energy, the number of protons used can be found. This was done using the following equation,

$$\mathrm{NP}_{guess} = \sum_{k=1}^{N_v} (D_r(V_k)\Delta x\Delta y\Delta z\rho_k)/E, \tag{3.4}$$

where $D_r(V_K)$ describes the planned dose distribution provided by RayStation in voxel V_k. Δx, Δy and Δz are the voxel sizes in the respective directions, ρ_k is the density of the CT volume in voxel V_k and E is the planned energy by RayStation. An overview of the optimization bounds is given in Table 3.1.

Table 3.1: Overview of the optimization bounds.

Symbol	Lower bound	Upper bound
E (MeV)	$0.5E_{BDL}$	$1.5E_{BDL}$
σ_E (MeV)	0.0	$\sigma_{E,BDL}$+5.0
NP	$0.8NP_{guess}$	NP_{guess}
σ_x (cm)	0.0	10.0
σ_{Ω_x} (rad)	0.0	1.0E-2
ϱ	0.0	1.0
γ_i, i=[1,2,..,8]	0.0	1.0

Where the subscript 'BDL' refers to the value found in the HPTC BDL.

For the planned spots including range shifters, the initial guess provided to the minimization function needed to be extracted from the RayStation dose distribution, as there was no BDL available to use as a baseline. To extract these initial guesses three steps were taken:

- To extract the mean spot energy, an optimization was performed, where the objective function was the sum of the squared difference of the IDD. Only the mean spot energy was optimized, while the other beamlet parameters remained constant.
- A similar optimization was used to find an initial guess for both the number of protons and the energy spread, using the newly found estimate for the mean spot energy. The sum of the squared difference of the IDD around the Bragg peak was used as an objective function.
- The lateral spread was determined by fitting a 1D Gaussian function over the lateral profile of the spot in the x direction at the entrance of the CT volume.

The bounds of these extracted initial guesses could be stricter than for the cases without range shifters, as these initial guesses were reasonable. Arbitrary chosen values were used for the initial guess of the angular spread

and correlation. The upper bound for the angular spread had to be increased, as an effect of the range shifter is a larger angular spread [19]. An overview of the adjusted bounds can be found in Table 3.2.

Table 3.2: Overview of the optimization bounds including range shifters.

Symbol	Lower bound	Upper bound
E (MeV)	E_{guess}-0.5	E_{guess}+0.5
σ_E (MeV)	$\sigma_{E,guess}$-0.5	$\sigma_{E,guess}$+0.5
NP	$0.9NP_{guess}$	$1.03NP_{guess}$
σ_x (cm)	$\sigma_{x,guess}$-0.2	$\sigma_{x,guess}$+0.2
σ_{Ω_x} (rad)	0.0	1.0E-1
ϱ	0.0	1.0
γ_i, i=[1,2,..,8]	0.0	1.0

Where the subscript 'guess' indicates the value of the parameter found from the above described methods to extract this information from the RayStation planned dose distribution.

3.1.5. Optimizer

The optimizer that was used was the Python minimize function from the SciPy library [28]. This function takes Equation 3.1 or Equation 3.2 as input to minimize. Also, the first guess of what the optimization parameters should be, which was described in subsection 3.1.4, is provided as input. Then it takes the method of optimization as input. In this thesis, the method trust-constr was chosen. This is a trust region based algorithm that is compatible with bounds and constraints. The bounds and the constraint were inputted to the optimizer, and the maximum number of iterations was set to 300. This was done after observing that after 300 iterations the change in objective was very small. The other input options were set to their default values.

3.1.6. Energy domain discretization

The clinical range of proton beams is generally 1 MeV to 244 MeV. The energy domain of YODA was extended from 200 MeV to 244 MeV. To expand the energy domain the group size and the number of energy groups had to be adjusted. The group size was held constant at 0.5 MeV, which yielded 486 groups for a maximum energy of 244 MeV.

Computations with spot energies close to the upper bound of the energy domain are not always reliable, due to the energy spread of a spot some of the energy that should be deposited will be neglected, as this energy was higher than the upper bound of the energy domain. Energies up to 230 MeV were used, as the magnitude of the energy spread was found to be roughly in the range of 1 to 4 MeV depending on the planned spot.

3.2. Performed experiments

3.2.1. Plan comparisons

To compare the planned dose against the calibrated YODA dose, RayStation was used to generate simple plans. These plans consisted of water boxes of 100 mm by 300 mm by 100 mm as the CT volume, and no range shifter was present in any of the plans. Two types of plans were used in this experiment.

The first type contained a single spot of 100 MeV, originating for each plan from a different gantry angle. The angles that were used where 10°, 20°, 30°, 60°, 70°, 80° and 90°.

The second type consisted of a target cube of 20 mm by 20 mm by 20 mm, centered in the CT volume, that was being irradiated. In one plan this cube was irradiated by one beam, containing multiple energy layers and spots, under a 0° gantry angle. There were two plans where the cube was irradiated by two beams, either from a 60° and a 300° gantry angle or from a 90° and a 270° gantry angle. Lastly, there was a plan where four beams irradiated the cube coming from 60°, 120°, 240° and a 300° gantry angle.

To account for angled beams, beam splitting as described by Burlacu et al. [16] is used, which is an approximation that also can be used to account for lateral heterogeneities. This is an approximation where a beam is split up into subspots, where the position of these subspots was prescribed to be on concentric rings, with the center being the central axis of the original spot. Then, the spatial spread and number of protons were optimized. The beam splitting scheme that was used for this experiment was [1,6,6,6,12,12,12]. Each number

in this scheme describes the number of subspots placed on that ring, with the first number being the center and the last number being the outer ring. The BDL file created by the calibration procedure was used to yield the YODA dose.

3.2.2. Asymmetrical spot error

To test what the effect is in the delivered dose when assuming a symmetrical spot instead of an elliptical spot, the Fermi-Eyges solution for an asymmetrical spot had to be derived. Then the effect of this asymmetrical spot on the integrated Fermi-Eyges flux, Ψ_{FE}, was derived. For several combinations of spatial spreads, angular spreads and correlations, the difference in Ψ_{FE} between the symmetrical case and the asymmetrical case was calculated using $\Delta\Psi_{FE} = \Psi_{FE,Symm} - \Psi_{FE,Asymm}$. For the symmetrical case, the mean was taken of the spatial spread, angular spread and correlation, as this is what is done in YODA. The difference in Ψ_{FE} could be directly related to the difference in dose, using the Equation 2.26. From this difference in Ψ_{FE}, the difference relative to the maximum integrated Fermi-Eyges flux in the symmetrical case was calculated. This calculation was done at the entrance of the CT volume as well as at the Bragg Peak. The combinations of spatial spread, angular spread and correlation were extracted from the BDL file created for MC^2 and measurements at HPTC, as these are realistic combinations for those parameters.

3.2.3. Systematic log file error

To explore the effect of systematic errors in the log files on this QA tool, disruptions were added manually to the YODA input. The plan used for this experiment was the simple water box plan, in which a cube of 20 mm by 20 mm by 20 mm centered in the middle of the CT volume is irradiated from a 0° angle beam. The central beam axis is along the y direction and the x,z plane is the lateral plane. The irradiated cube will be referred to as the target. Again, beam splitting was applied as described by Burlacu et al. [16]. In this experiment, the beam splitting scheme [1,6,6,6] was used, due to time limitations and considering the number of spots. The dose distribution found by YODA without perturbation was taken as a reference.

Log files contain information on spot position and MU, thus these were the quantities in which the perturbations were added. For the x and z directions, perturbations of 0.8, 0.6, 0.4 and 0.2 mm were added in both the negative and positive axis. This was based on values found in the literature. A publication by Li et al. [35], found that the maximum deviation in the log file spot position compared to the measured spot position was 0.65 mm. Toscano et al. [13] found that the standard deviation in spot position found for a 100 MeV spot with varying MU was 0.54 mm while the maximum systematic shift could go up to 1.5 mm. However, the treatment system in this publication can deliver a beam within an accuracy of 0.2 mm, therefore Toscano et al. [13] suggest that this uncertainty in the log file spot position should be taken into account to ensure that deviations in spot position are not misinterpreted. Toscano et al. [13] suggest that a model of systematic and random errors in the spot position of the log files should be made and included in the reconstructed dose calculations. This model of systematic errors is dependent on energy, planned spot position and MU. Ates et al. [36] found a systematic shift of 0.005 ± 0.189 mm in x and 0.125 ± 0.175 mm in y during the trend analysis of six years of treatment data. Li et al. [35] claim that the deviation in MU in log files to the planned MU is smaller than 1%. Ates et al. [36] found a percentage difference in MU of $0.07\% \pm 3.53\%$. Perturbations of 1%, 0.75%, 0.5% and 0.25% were added, again both positive and negative. Also, the effect of perturbation in energy was explored by adding and subtracting 0.1%, 0.075%, 0.05% and 0.025% of the energy.

First, the whole target cube was perturbed with the above-discussed perturbations, then an experiment was performed where each energy layer was perturbed with a random perturbation. This perturbation was randomly selected from a uniform distribution where the values ranged between -0.8 mm to 0.8 mm for x and z, -1% to 1% for MU and -0.1% to 0.1% for energy. This experiment was repeated ten times for each quantity and the mean and standard deviation for these experiments were calculated.

3.3. Comparison metrics

To test the validity of both the optimizations and the experiments that were performed, different tools were used. For the calibration and the simple water box plan comparisons, first a visual inspection of the IDD and the 1D lateral profile at different depths was performed. Second, 2D dose slices were plotted from different perspectives and analyzed. Lastly, the gamma index was utilized to create a passing rate. The aim was an as high as possible passing rate. The used acceptance criteria for the gamma index were 1 mm, 1% and a cutoff of 10%.

For the investigation of the effect of an asymmetrical spot, the difference of Ψ_{FE} between the asymmetrical and symmetrical case, relative to the maximum of the symmetrical case integrated Fermi-Eyges flux, was calculated and plotted at both entrance and the Bragg peak. The maximum difference relative to the maximum symmetrical integrated Fermi-Eyges flux was calculated. The mean difference relative to the maximum symmetrical integrated Fermi-Eyges flux inside a square centered around the beam was also calculated. The width of the square was found by fitting a Gaussian function over the profile of the integrated Fermi-Eyges flux and taking four times the spread, σ, of this fitted Gaussian. This mean value, inside this square, gives an idea of the magnitude of the difference introduced by assuming symmetry around the central beam axis.

Lastly, to investigate the effect of systematic errors in the log file, the passing rate was calculated using the unperturbed dose as a reference, and again using the 1 mm, 1% acceptance criteria with a 10% cutoff. Also, the difference in dose relative to the maximum dose of the unperturbed dose was calculated and plotted. From this, the maximum difference was calculated, as well as the mean in the target cube. This mean value can give insight as to what the effect on the target will be of such a perturbation.

4

Results and discussion

In this section, the results of the performed experiments will be presented and discussed. Firstly, the results of the calibrations will be discussed, and then the results of the plan comparisons will be presented. The results of the asymmetrical spot solution to the Fermi-Eyges equation will be discussed next and lastly, the results of the investigation of the effect of systematic log file errors will be discussed.

4.1. Calibration results

The passing rates achieved with the calibration procedure for the no range shifter case and the 2 cm, 3 cm and 5 cm range shifters are shown in Figure 4.1, as a function of planned energy. This planned energy is the energy of the beam without the energy reduction as a result of the range shifter included.

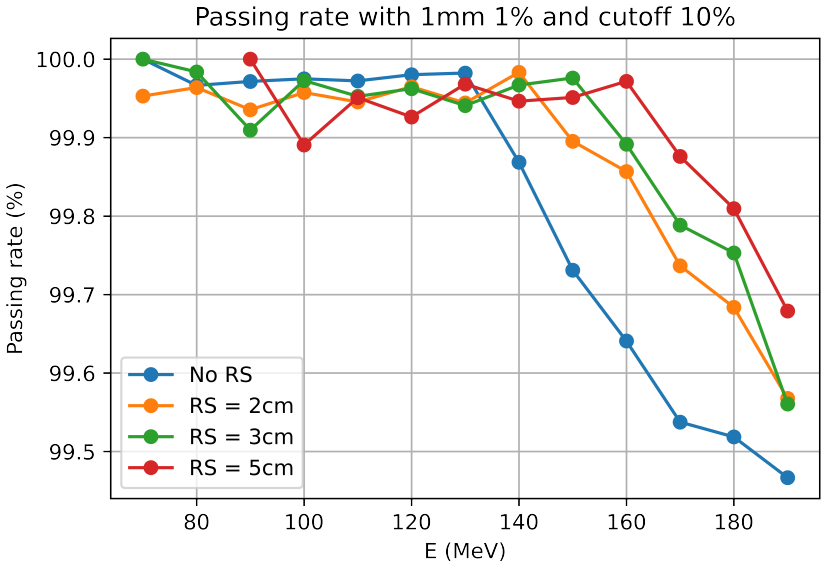

Figure 4.1: The passing rates of the YODA calibrated dose, with the RayStation planned dose as a reference, against planned energy for no range shifter, 2cm, 3cm and 5cm range shifters.

As shown in Figure 4.1, the lowest passing rate found from the calibration procedure is 99.47% for the no range shifter case at 190 MeV planned energy. In Figure 4.2, the passing rate of the calibrated no range shifter case is plotted against energy, along with the passing rate obtained when using the BDL file made for MC^2 and HPTC measurements. As shown in Figure 4.2, the passing rates for the optimized BDL are much higher than the passing rates found when using the BDL file made specifically for MC^2 and measurements at HPTC.

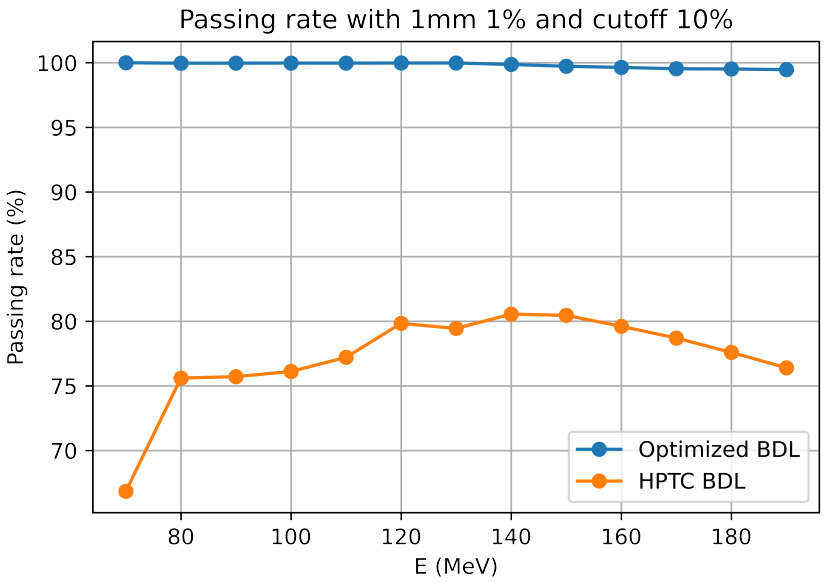

Figure 4.2: The passing rate against planned energy for the calibrated YODA dose and the YODA dose, using the HPTC BDL file, with the planned RayStation dose as reference.

There seems to be a trend that for higher planned energy the passing rate goes down in Figure 4.1. Figure 4.3 shows the IDD of the calibrated dose yielded by YODA and the RayStation planned dose for 100 MeV and 190 MeV planned energy with no range shifter present.

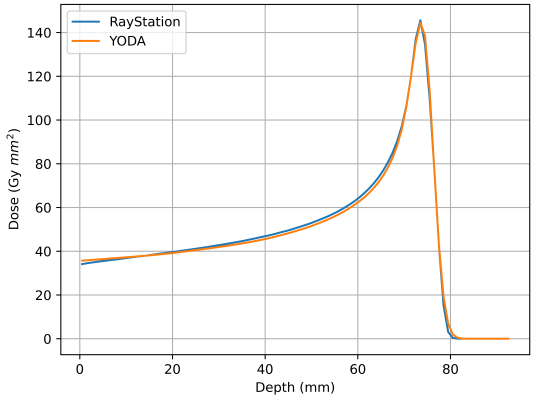

(a) The integral depth dose curve for the YODA calibrated dose and the RayStation planned dose against depth for 100 MeV planned energy.

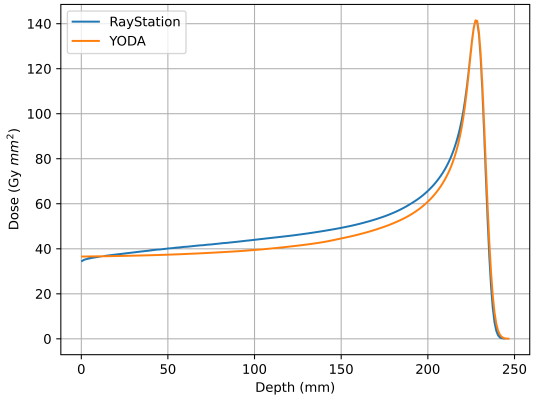

(b) The integral depth dose curve for the YODA calibrated dose and the RayStation planned dose against depth for 190 MeV planned energy.

Figure 4.3: The integral depth dose curve for the YODA calibrated dose and the RayStation planned dose against depth for 100 MeV planned energy and 190 MeV planned energy.

In Figure 4.3b it can be seen that for the 190 MeV case, the entrance region is underestimated by the YODA calibration result, whereas this region is better matched for the 100 MeV case as shown in Figure 4.3a. This could explain the decreasing passing rate for higher energies in Figure 4.1. The reason why this region is less well matched for higher energies could be explained by nuclear interactions, as the effect of nuclear interaction on the beam becomes more significant for higher energies. In YODA, nuclear interactions and the resulting secondaries are not tracked, as is done in Monte Carlo-based dose engines. An approximation, to deal with nuclear interactions, was introduced to YODA for the purpose of this thesis. A quantity γ, describing the fraction of locally deposited dose due to nuclear interaction, was added in Ψ_{FP}, and was optimized at 9 points of beam energy. However, this is still a crude approximation of reality, which can explain why there is not a better match between the YODA and RayStation dose. This approximation added 9 additional optimization parameters increasing the computation time of the calibration significantly. The calibration only has to be performed

once to create the BDL files, therefore the increase in computation time is not a major issue.

From Figure 4.1 it can be seen that the passing rates for the calibration procedure including range shifters are higher then without range shifters. This might be explained by the fact that the optimization bounds were stricter for the range shifter cases and the initial guesses provided to the optimizer were extracted from the RayStation data instead of using the HPTC BDL file resulting in a faster convergence of the optimization.

4.2. Plan comparisions

For a few simple water box plans, a comparison was performed between the planned RayStation dose and the calibrated YODA dose. The used plans were described in Subsection 3.2.1. The passing rates retrieved from these plan comparisons are shown in Table 4.1.

Table 4.1: Passing rates for simple plan comparisons using 1% 1 mm acceptance criteria and 10% cutoff for the gamma index.

Plan	Passing rate
Single spot 0° gantry angle	99.97%
Single spot 10° gantry angle	100.0%
Single spot 20° gantry angle	88.15%
Single spot 30° gantry angle	90.41%
Single spot 60° gantry angle	92.59%
Single spot 70° gantry angle	92.81%
Single spot 80° gantry angle	92.42%
Single spot 90° gantry angle	92.24%
Cube 0° gantry angle	84.06%
Cube 60° and 300° gantry angle	93.85%
Cube 90° and 270° gantry angle	90.69%
Cube 60°, 120°, 240° and 300° gantry angle	95.32%

Notable is that most of the passing rates from the single spot angled plans are much lower than the 0° gantry angle plan that was used for the calibration, which had a passing rate of 99.97%. This might be due to limitations in the beam splitting scheme for angled beam entrance. Beam splitting is an approximation typically used to address lateral heterogeneity. The gantry angle results in an angled entrance at the CT volume air interface, the projection of the beam on the surface of the CT volume is then no longer a circle, as assumed, but an ellipse. This causes beams incoming at the corner of the CT volume to have a lower passing rate compared to beams coming in at a small gantry angle. A 2D dose plot, at the central beam axis, of a 100 MeV, no range shifter, single spot, under a gantry angle of 10° and a gantry angle of 20°, is shown in Figure 4.4.

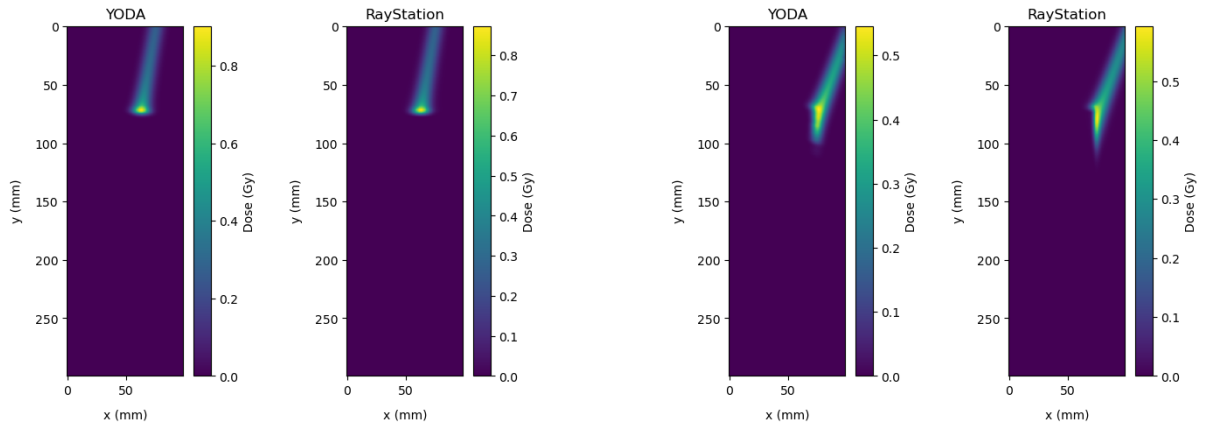

(a) 2D plot at the central beam axis of a 100 MeV spot without a range shifter at a 10° gantry angle of both the YODA dose and the RayStation planned dose.

(b) 2D plot at the central beam axis of a 100 MeV spot without a range shifter at a 20° gantry angle of both the YODA dose and the RayStation planned dose.

Figure 4.4: Comparision of the YODA dose against the RayStation planned dose for a 100 MeV single spot from a 10° gantry angle and a 20° gantry angle.

In Figure 4.4b the effect on the spot of entering the CT volume at the corner is clearly visible, whereas the agreement between RayStation and YODA is much higher in Figure 4.4a.

Also noteworthy is the 90° case. As the beam is perpendicular to the CT surface, just as in the 0° case, one would expect similar results. However, the passing rate of the 90° case is significantly lower, 92.24% compared to 99.97% of the 0° case. This can be explained by the fact that the CT volume is not a cube, it does not have sides of equal length. Due to the volume being longer in the y direction than in the x and z direction, there is more distance between the isocenter and the CT volume surface when the gantry angle is 0° compared to 90°. The boundary conditions of YODA are at the CT volume surface, whereas the RayStation plan is defined in air at the isocenter. RayStation therefore takes into account the effect of the extra distance between the isocenter and the CT volume surface for 0° compared to 90°, whereas YODA does not. The spot size increases from exiting the nozzle with depth due to multiple scattering [19] and perhaps more importantly due to the divergence the beam has. According to the commissioning procedure for MC^2 [31] the divergence of the beam is constant with depth, and the correlation can also increase with depth. Therefore if the distance between the isocenter and the CT volume surface is shorter, the beam will be broader at the CT volume surface than when this distance would be larger, due to the geometrical spread.

A comparison of the lateral profile, at the entrance of the CT volume between YODA and RayStation is shown in Figure 4.5 for the 100 MeV single spot incoming from gantry angles 0° and 90°.

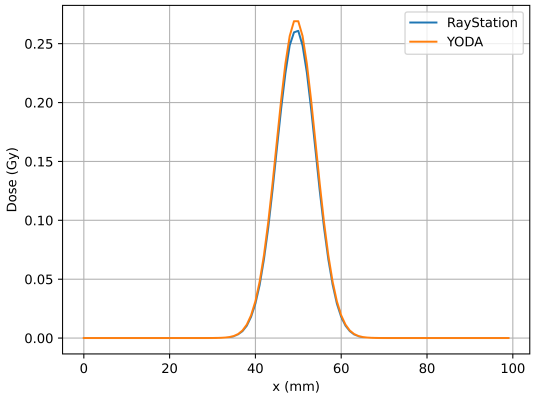

(a) Comparision of the lateral profile at the entrance of the CT volume of a 100 MeV spot without a range shifter at a 0° gantry angle between the YODA dose and the RayStation planned dose.

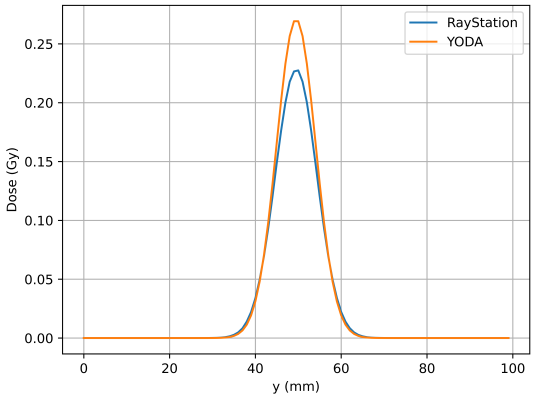

(b) Comparision of the lateral profile at the entrance of the CT volume of a 100 MeV spot without a range shifter at a 90° gantry angle between the YODA dose and the RayStation planned dose.

Figure 4.5: Comparison of the lateral profile of the YODA dose and the RayStation planned dose for a 100 MeV single spot from a 0° gantry angle and a 90° gantry angle.

From Figure 4.5a it is clear that the difference in spot size between YODA and RayStation is very small at the entrance of the CT volume for a 0° gantry angle, whereas in Figure 4.5b the RayStation spot has a slightly bigger spot size at the entrance and a lower dose at the central beam axis compared to YODA for a 90° gantry angle. This difference in lateral profile for the RayStation dose between the 0° and 90° gantry angle can be explained by the additional distance between the isocenter and the CT volume surface at a 0° gantry angle compared to a 90° gantry angle caused by the CT volume shape and the geometrical spread of the beam. The BDL files created in this thesis are thus specific for the isocenter to CT volume surface distance used in the reference data.

For the 10° case the passing rate was slightly higher, 100%, than the passing rate for the 0° case, 99.97%. Possibly, this small improvement in passing rate is caused coincidentally by a combination of the differences in dose from the calibrating procedure and the effect of the above-described errors induced by the slight angle of the beam.

Figure 4.6 shows a comparison of the dose at the central beam axis of YODA and RayStation for the cubes plans, as listed in Table 4.1, irradiated by either 1,2 or 4 beams. It appears that irradiating a target cube using more beams with different angles leads to a higher passing rate, 95.32% for the 4 beam case than using fewer beams, 84.06% for the single beam case, although from visual inspection of Figure 4.6 this is not as obvious. This may be explained by the fact that at some voxels in the geometry, YODA underestimates the dose, while in others, it overestimates the dose compared to the planned RayStation dose. When multiple beams with different angles

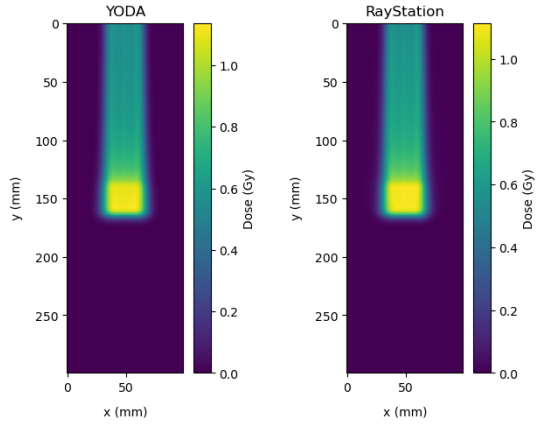

(a) 2D plot at the central beam axis of the YODA and RayStatation dose of a cube irradiated by one beam with gantry angle 0°.

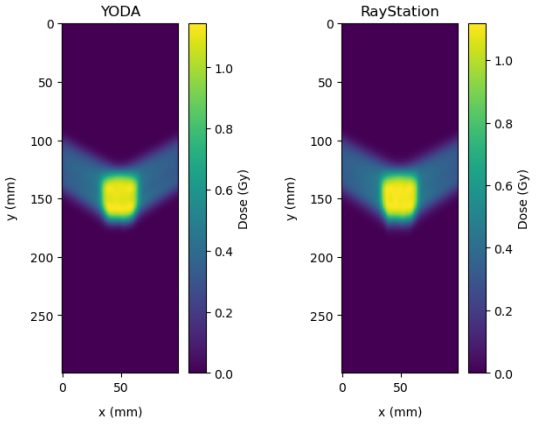

(b) 2D plot at the central beam axis of the YODA and RayStatation dose of a cube irradiated by two beams with gantry angles 60° and 300°.

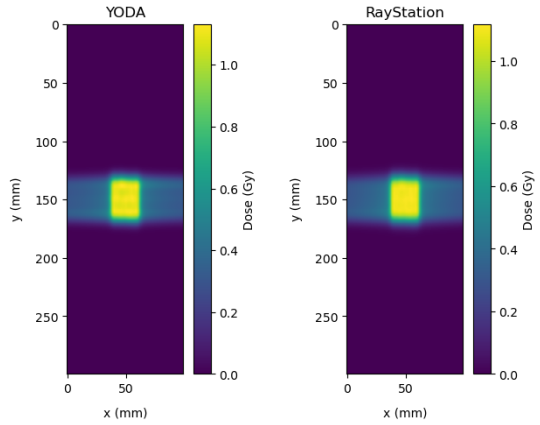

(c) 2D plot at the central beam axis of the YODA and RayStatation dose of a cube irradiated by two beams with gantry angles 90° and 270°.

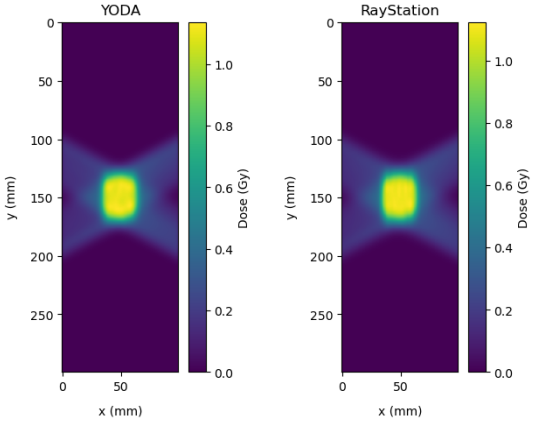

(d) 2D plot at the central beam axis of the YODA and RayStatation dose of a cube irradiated by four beams with gantry angles 60°, 120°, 240° and 300°.

Figure 4.6: 2D plot at the central beam axis of the YODA and RayStation dose for a 20 mm by 20 mm by 20 mm centered in the CT volume irradiated by either 1, 2, or 4 beams with different gantry angles.

are used and they overlap at some voxels, it is possible that some of this underestimating and overestimating cancel out, leading to a higher passing rate. This higher passing rate can be deceiving as the individual beams are not as well matched as the combination of the beams and therefore the accuracy of the model is lower then the passing rates lead to believe.

4.3. Asymmetrical spot error

In this section, the results of the derivation of the asymmetrical spot solution to the Fermi-Eyges equation will be presented and discussed, as well as the effect of the asymmetry on the integrated Fermi-Eyges flux.

4.3.1. Derivation of the asymmetrical spot solution to the Fermi-Eyges equation

The solution of the Fermi-Eyges equation, described in Equation 2.15, is a solution for a symmetrical spot. However, spots are not necessarily symmetrical. To account for asymmetrical spots, the Fermi-Eyges equation needed to be solved for non-symmetrical initial conditions. Similar steps were taken as in Subsection 2.3.1.2, as the only difference is that there are different initial conditions for x and y. The initial condition corresponding to the x direction was

$$H(0,x,\Omega_x) = C_1 \exp\left(-(a_1 x^2 + a_2 x\Omega_x + a_3\Omega_x^2)\right). \tag{4.1}$$

The coefficients a_1, a_2 and a_3 can be found by

$$a_1 = \frac{1}{2(1-\varrho_x^2)\sigma_x^2}, \quad a_2 = -\frac{\varrho_x}{(1-\varrho_x^2)\sigma_x\sigma_{\Omega_x}}, \quad a_3 = \frac{1}{2(1-\varrho_x^2)\sigma_{\Omega_x}^2}, \tag{4.2}$$

where ϱ_x describes the correlation coefficient between x and Ω_x, and σ_x and σ_{Ω_x} are the standard deviations of x and Ω_x respectively.

The initial condition corresponding to the y direction was then

$$H(0,y,\Omega_y) = C_2 \exp\Big(-(a_4 y^2 + a_5 y\Omega_y + a_6\Omega_y^2)\Big) \tag{4.3}$$

The coefficients a_4, a_5 and a_6 can be found by

$$a_4 = \frac{1}{2(1-\varrho_y^2)\sigma_y^2}, \quad a_5 = -\frac{\varrho_y}{(1-\varrho_y^2)\sigma_y\sigma_{\Omega_y}}, \quad a_6 = \frac{1}{2(1-\varrho_y^2)\sigma_{\Omega_y}^2}, \tag{4.4}$$

where ϱ_y describes the correlation coefficient between y and Ω_y, and σ_y and σ_{Ω_y} are the standard deviations of y and Ω_y respectively.

The full derivation is shown in Appendix A. The solution was found to be

$$\begin{aligned}\phi_{FE}(\boldsymbol{r},\hat{\boldsymbol{\Omega}}) = \frac{C_1}{\sqrt{D_1}}\frac{C_2}{\sqrt{D_2}} &\frac{\exp\big((A_2(z)\Omega_x^2 - 2A_1(z)\Omega_x x + A_0(z)x^2)/(4A_1^2(z) - 4A_0(z)A_2(z))\big)}{\sqrt{4A_0(z)A_2(z) - 4A_1^2(z)}\sqrt{4A_3(z)A_5(z) - 4A_4^2(z)}} \\ &\exp\Big((A_5(z)\Omega_y^2 - 2A_4(z)\Omega_y y + A_3(z)y^2)/(4A_4^2(z) - 4A_3(z)A_5(z))\Big),\end{aligned} \tag{4.5}$$

with the following coefficients:

$$A_0(z) = \frac{a_1}{D_1} + \int_0^z \overline{\Sigma_{tr}}(\eta)\mathrm{d}\eta, \tag{4.6}$$

$$2A_1(z) = -\frac{a_2}{D_1} + \frac{2a_1}{D_1}z + 2\int_0^z (z-\eta)\overline{\Sigma_{tr}}(\eta)\mathrm{d}\eta, \tag{4.7}$$

$$A_2(z) = \frac{a_3}{D_1} - \frac{a_2}{D_1}z + \frac{a_1}{D_1}z^2 + \int_0^z (z-\eta)^2\overline{\Sigma_{tr}}(\eta)\mathrm{d}\eta, \tag{4.8}$$

$$A_3(z) = \frac{a_4}{D_2} + \int_0^z \overline{\Sigma_{tr}}(\eta)\mathrm{d}\eta, \tag{4.9}$$

$$2A_4(z) = -\frac{a_5}{D_2} + \frac{2a_4}{D_2}z + 2\int_0^z (z-\eta)\overline{\Sigma_{tr}}(\eta)\mathrm{d}\eta, \tag{4.10}$$

$$A_5(z) = \frac{a_6}{D_2} - \frac{a_4}{D_2}z + \frac{a_5}{D_2}z^2 + \int_0^z (z-\eta)^2\overline{\Sigma_{tr}}(\eta)\mathrm{d}\eta, \tag{4.11}$$

$$\tag{4.12}$$

and $D_1 = 4a_1a_3 - a_2^2$, $D_2 = 4a_4a_6 - a_5^2$.

When $z = 0$ is filled in the solution, the initial condition is obtained. However, when filling in a symmetrical spot, the solution found by Gebäck and Asadzadeh [24] is not obtained. The solution by Gebäck and Asadzadeh [24] likely contained a typo. The differences will be discussed in the next subsection, as the difference introduced in the integrated Fermi-Eyges flux is relevant for dose calculations.

4.3.2. Error in integrated Fermi-Eyges flux

To test the effect of an asymmetrical spot compared to a symmetrical spot, the integrated Fermi-Eyges flux will be examined. A difference in the Fermi-Eyges flux directly translates to a difference in deposited energy, as can be seen in Equation 2.26. The integrated Fermi-Eyges flux is described in Equation 2.24. Because the domain of Ω_x and Ω_y was extended to $(-\infty,\infty)$, the same can be done with the integrated Fermi-Eyges flux, leading to the following equation [15]

$$\Psi_{FE}(\boldsymbol{r}) = \int_{4\pi}\mathrm{d}\hat{\boldsymbol{\Omega}}\phi_{FE}(\boldsymbol{r},\hat{\boldsymbol{\Omega}}) \approx \int_{-\infty}^{\infty}\int_{-\infty}^{\infty}\mathrm{d}\Omega_x\mathrm{d}\Omega_y\phi_{FE}(\boldsymbol{r},\hat{\boldsymbol{\Omega}}) \tag{4.13}$$

As the Fermi-Eyges flux is separable in x and y this leaves

$$\Psi_{FE}(\boldsymbol{r}) \approx \int_{-\infty}^{\infty}\int_{-\infty}^{\infty} H(z,x,\Omega_x)H(z,y,\Omega_y)\mathrm{d}\Omega_x\mathrm{d}\Omega_y. \tag{4.14}$$

Where $H(z,x,\Omega_x)$ and $H(z,y,\Omega_y)$ are both Gaussian functions. The integrals are solved and the Fermi-Eyges flux is normalized, resulting in the following expression

$$\Psi_{FE}(\boldsymbol{r}) \approx \frac{1}{4\pi\sqrt{A_2(z)A_5(z)}}\exp\left(\frac{-x^2}{4A_2(z)}+\frac{-y^2}{4A_5(z)}\right) \tag{4.15}$$

For a symmetrical spot $A_2(z) = A_5(z)$ applies. As mentioned in the previous section there are some differences between the solution by Gebäck and Asadzadeh [24] and the solution presented in the previous subsection. For Equation 2.24 to result in the same symmetrical integrated Fermi-Eyges flux as presented here, the coefficients that were published as $\overline{\Theta^2}(0) = \frac{2a_3}{D}$, $\overline{\Theta\xi}(0) = \frac{a_2}{D}$ and $\overline{\xi^2}(0) = \frac{2a_1}{D}$ need to be $\overline{\Theta^2}(0) = \frac{2a_1}{D}$, $\overline{\Theta\xi}(0) = \frac{-a_2}{D}$ and $\overline{\xi^2}(0) = \frac{2a_3}{D}$ and there needs to be a factor of 2 in front of the integral term of $\overline{\xi^2}(z)$, which is described by Equation 2.18. It might be that the notation of a factor 1/2 is missing in front of $\overline{\Sigma_{tr}}$ in the definition of the Fermi-Eyges equation by Gebäck and Asadzadeh [24] which could explain this missing factor of 2 in the integral term of $\overline{\xi^2}(z)$ compared to the solution presented in this section.

The difference in Ψ_{FE} between a symmetrical spot and an asymmetrical spot was calculated both at the entrance of the CT volume and the Bragg peak (BP). This was done for the spatial spread, angular spread and correlation found in the BDL created for HPTC and MC^2 for energies ranging from 70 MeV to 190 MeV. As these BDLs were constructed based on measurements at HPTC, the spatial spread, angular spread and correlation should be fair approximations of what is used in clinical practice. The values found during the calibration procedure in this thesis could not be used as symmetry was assumed during the calibration and the parameters were energy-dependent. The difference was expressed relative to the maximum integrated Fermi-Eyges flux of the symmetrical spot. Both the mean of $|\Delta\Psi_{FE}|$, around the central beam axis, and the maximum of $|\Delta\Psi_{FE}|$, relative to the maximum of the symmetrical Ψ_{FE}, are shown in Table 4.2.

Table 4.2: The effect of assuming symmetrical spots on the integrated Fermi-Eyges flux relative to the maximum integrated Fermi-Eyges flux of the symmetrical case.

σ_x (cm)	σ_{Ω_x} (rad)	ϱ_x	σ_y (cm)	σ_{Ω_y} (rad)	ϱ_y	Mean $\lvert\Delta\Psi_{FE}\rvert$, z=0	Max $\lvert\Delta\Psi_{FE}\rvert$, z=0	Mean $\lvert\Delta\Psi_{FE}\rvert$, z=BP	Max $\lvert\Delta\Psi_{FE}\rvert$, z=BP
0.4173	0.007091	0.3967	0.3695	0.006385	0.7785	2.075%	4.728%	0.6198%	0.9683%
0.4238	0.006958	0.2005	0.3934	0.006197	0.4857	1.215%	2.842%	0.4710%	1.107%
0.4189	0.006327	0.1427	0.3742	0.005387	0.5797	1.926%	4.371%	1.098%	2.390%
0.3862	0.003833	0.5732	0.3671	0.004847	0.5381	0.8426%	1.896%	1.044%	2.367%
0.3811	0.004569	0.2673	0.3441	0.003985	0.7153	1.678%	3.890%	0.9685%	2.313%
0.3893	0.005091	0.01700	0.3226	0.003240	0.9446	3.071%	7.533%	4.218%	6.986%
0.3576	0.003773	0.2634	0.3260	0.003992	0.4742	1.582%	3.555%	1.170%	2.821%
0.3481	0.003323	0.2868	0.3279	0.004177	0.3101	1.013%	2.261%	2.170%	4.915%
0.3444	0.003265	0.2398	0.3307	0.004695	0.1192	0.6853%	1.520%	3.314%	7.728%
0.3450	0.003519	0.1033	0.3204	0.004588	0.1110	1.252%	2.826%	3.051%	7.251%
0.3342	0.002333	0.3466	0.3071	0.004025	0.2089	1.410%	3.238%	4.957%	12.05%
0.3404	0.003356	0.007080	0.2985	0.003730	0.2554	2.201%	5.129%	2.290%	5.685%
0.3401	0.003456	-0.05678	0.3018	0.004170	0.1003	2.003%	4.644%	3.214%	7.671%

The mean of $|\Delta\Psi_{FE}|$ was calculated inside a square centered around the spot with a width of 4σ, which was fitted from the symmetrical Ψ_{FE}. The values range from 0.6853% to 3.071% at the entrance of the CT volume, and from 0.4710% to 4.957% at the Bragg peak, depending on the combination of parameters. This difference can be directly related to the difference in dose in the same area, $\Delta E = \int_{V_k} \mathrm{d}V\Delta\Psi_{FE}(\boldsymbol{r})\Psi_{FP}(z)$, and is significant.

In Figure 4.7 three cases from Table 4.2 are shown. Each case has its own distinct pattern at the Bragg peak. In all three cases, shown in Figure 4.7, the difference in σ_x and σ_y has a clear effect at the entrance of the CT volume. The asymmetrical spot is compared to a symmetrical spot that uses the mean of the parameters shown in Table 4.2. In all three cases, σ_x is bigger than the mean, and it is shown that the asymmetrical spot is wider in x and smaller in y as was expected.

All three distinct patterns for the difference in Ψ_{FE} at the Bragg peak shown in Figure 4.7, can be explained by the fact that the angular spread and the correlation both influence the shape of the spot at the Bragg peak. A higher correlation results in a more spread-out spot at the Bragg peak. A bigger angular spread will also cause

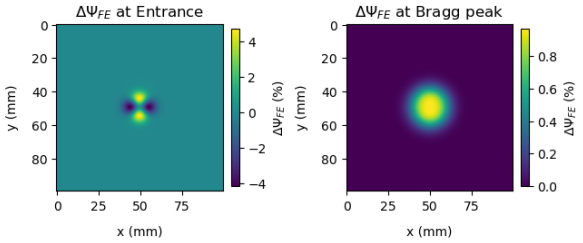

(a) 2D plot of the lateral plane of $\Delta\Psi_{FE}$ at entrance of the CT volume and at the Bragg Peak for $\sigma_x = 0.4173$ cm, $\sigma_{\Omega_x} = 0.007091$, $\text{corr}_x = 0.3967$, $\sigma_y = 0.3695$ cm, $\sigma_{\Omega_y} = 0.006385$, $\text{corr}_y = 0.7785$.

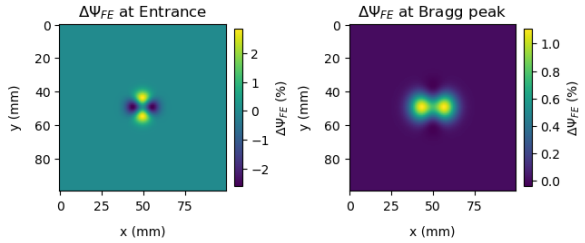

(b) 2D plot of the lateral plane of $\Delta\Psi_{FE}$ at entrance of the CT volume and at the Bragg Peak for $\sigma_x = 0.4238$ cm, $\sigma_{\Omega_x} = 0.006958$, $\text{corr}_x = 0.2005$, $\sigma_y = 0.3934$ cm, $\sigma_{\Omega_y} = 0.006197$, $\text{corr}_y = 0.4857$.

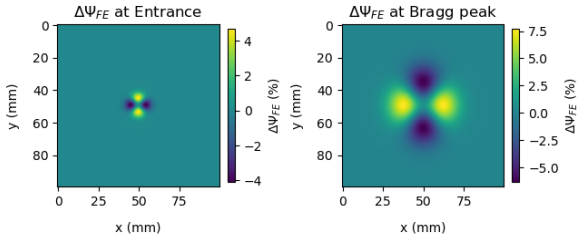

(c) 2D plot of the lateral plane of $\Delta\Psi_{FE}$ at entrance of the CT volume and at the Bragg Peak for $\sigma_x = 0.3401$ cm, $\sigma_{\Omega_x} = 0.003456$, $\text{corr}_x = -0.05678$, $\sigma_y = 0.3018$ cm, $\sigma_{\Omega_y} = 0.004170$, $\text{corr}_y = 0.1003$.

Figure 4.7: Comparison of the difference in Ψ_{FE} as a result of assuming spot symmetry for tree cases from Table 4.2, where the symmetrical case was yielded by averaging the parameters of the x and y direction.

a more spread-out spot at the Bragg peak. Because the mean of these parameters is taken for the symmetrical case, the effect of the asymmetrical spot could be one of the three patterns shown in Figure 4.7.

In Figure 4.7a, the difference of Ψ_{FE} between the asymmetrical spot and the symmetrical spot is a round-shaped pattern, indicating that the difference in the x and y directions is comparable. The difference in correlation is quite big for the x and y directions, namely 0.3818. The difference in angular spread is 0.000706. In the x direction, the angular spread is larger than the mean, and the correlation is smaller than the mean. In the y direction, the angular spread is thus smaller than the mean, and the correlation is then larger than the mean. This combination of parameters results in a comparable difference for the x and y direction with respect to the symmetrical case, and both being positive. In the x direction, the angular spread will broaden the spot, while the correlation will make the spot smaller compared to the symmetrical case. In the y direction, the angular spread will make the spot more narrow, while the correlation will broaden the spot compared to the symmetrical case. The total effect on the spot is very comparable for both the x and y directions, resulting in the pattern shown in Figure 4.7a.

Figure 4.7b shows, at the Bragg peak, a clear difference in the x direction, but not as distinct in the y direction. This can be explained by the fact that the correlation for y is larger than the mean and the angular spread for y is smaller than the mean. The difference between the correlation in x and y is 0.2852. The difference in angular spread in x and y is 0.000761. The difference in correlation is smaller compared to the case shown in Figure 4.7a, whereas the difference in angular spread is slightly higher. The reason why this case shows a different pattern at the Bragg peak, as shown in Figure 4.7b, compared to in Figure 4.7a, is because the magnitude of the differences in the angular spread and the correlation with respect to the mean values were different in this case. Since they both have influence on the spot size, a different pattern was yielded. In this case, because the angular spread was lower than the mean but the correlation larger than the mean in the y direction, the effect on Ψ_{FE} at the Bragg peak was similar to that of the symmetrical spot. The larger correlation causes a more spread-out spot, while the lower angular spread causes a smaller spot. In the x direction, this combination of parameters does not result in values of Ψ_{FE} that closely resemble the symmetrical case, hence resulting in a bigger difference in the x direction.

Figure 4.7c shows a comparable difference in both the x and y direction at the Bragg peak, but one is positive and one is negative. Here for the x direction, both the angular spread and the correlation are smaller than the mean. Therefore the spot will be less spread-out at the Bragg peak in the x direction than in the symmetrical

case. For the y direction, the angular spread and the correlation are both larger than the mean, thus the spot will be more spread out in the y direction at the Bragg peak than the symmetrical case.

4.4. Systematic log file error

In this section, an investigation was performed on the effect of a systematic error in a log file on the YODA dose reconstruction. This was done by perturbing the water box plan in which a cube, centered in the CT volume, is irradiated at a 0° gantry angle. This 20 mm by 20 mm by 20 mm cube will be referred to as the target. This plan was chosen because it contains multiple spots and energy layers but has small angles, which is closer to an actual patient plan than a single spot plan. As discussed in Section 4.2, irradiating under a gantry angle caused inaccuracies in the YODA dose, therefore an actual patient plan was not used for this experiment. First, the whole target cube, meaning every spot in the plan, was perturbed. This was done by shifting the spots in the x and z direction and perturbing the MU and energy. The passing rate was calculated using the unperturbed dose distribution as a reference. Also, the difference in dose between the perturbed and the unperturbed case was calculated, relative to the maximum of the unperturbed dose distribution. The results of the perturbation in x are displayed in Table 4.3, of z in Table 4.4, of the MU in Table 4.5, and lastly of the energy in Table 4.6.

Table 4.3: The effect of perturbing the whole target in x on the difference in dose relative to the maximum dose of the unperturbed case.

Perturbation in x	Mean $\lvert\Delta D\rvert$	Max $\lvert\Delta D\rvert$	Passing rate
-0.8 mm	0.2139%	7.498%	100%
-0.6 mm	0.1563%	5.625%	100%
-0.4 mm	0.1019%	3.751%	100%
-0.2 mm	0.05001%	1.872%	100%
0.2 mm	0.04866%	1.869%	100%
0.4 mm	0.09612%	3.743%	100%
0.6 mm	0.1433%	5.619%	100%
0.8 mm	0.1908%	7.496%	100%

Table 4.4: The effect of perturbing the whole target in z on the difference in dose relative to the maximum dose of the unperturbed case.

Perturbation in z	Mean $\lvert\Delta D\rvert$	Max $\lvert\Delta D\rvert$	Passing rate
-0.8 mm	0.2508%	7.506%	100%
-0.6 mm	0.1841%	5.626%	100%
-0.4 mm	0.1206%	3.747%	100%
-0.2 mm	0.05969%	1.870%	100%
0.2 mm	0.05836%	1.876%	100%
0.4 mm	0.1164%	3.755%	100%
0.6 mm	0.1745%	5.636%	100%
0.8 mm	0.2332%	7.512%	100%

Table 4.5: The effect of perturbing the whole target in MU on the difference in dose relative to the maximum dose of the unperturbed case.

Perturbation in MU	Mean $\lvert\Delta D\rvert$	Max $\lvert\Delta D\rvert$	Passing rate
-1%	0.9664%	1.000%	100%
-0.75%	0.7248%	0.750%	100%
-0.5%	0.4832%	0.500%	100%
-0.25%	0.2416%	0.250%	100%
0.25%	0.2416%	0.250%	100%
0.5%	0.4832%	0.500%	100%
0.75%	0.7248%	0.750%	100%
1%	0.9664%	1.000%	100%

Table 4.6: The effect of perturbing the whole target in E on the difference in dose relative to the maximum dose of the unperturbed case.

Perturbation in E	Mean $\lvert\Delta D\rvert$	Max $\lvert\Delta D\rvert$	Passing rate
−0.1%	0.1841%	3.620%	100%
−0.075%	0.1380%	2.717%	100%
−0.05%	0.09199%	1.813%	100%
−0.025%	0.04601%	0.9067%	100%
0.025%	0.04609%	0.9080%	100%
0.05%	0.09228%	1.813%	100%
0.075%	0.1386%	2.720%	100%
0.1%	0.1851%	3.624%	100%

Noticeable is that the passing rate is 100% for all the perturbations. This is because the acceptance criteria of 1% and 1 mm for the gamma index were employed. The perturbations were smaller than this criterion, and therefore the passing rate is 100%. To assess the effect of the induced error, the difference in the dose, ΔD, relative to the maximum dose of the unperturbed case was calculated. The maximum of $|\Delta D|$ of the whole CT volume was calculated, as well as the mean of $|\Delta D|$ was calculated in the target cube.

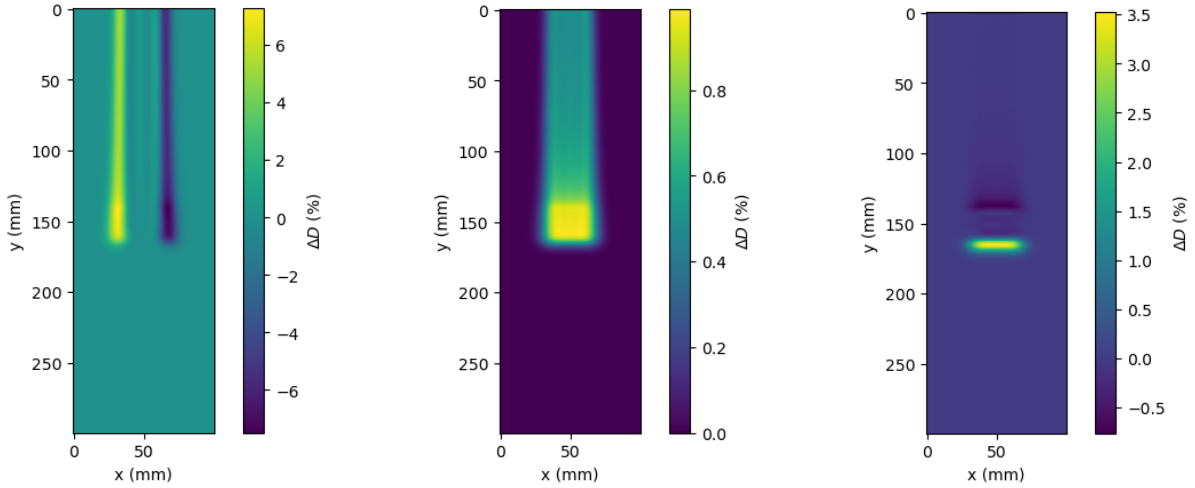

(a) 2D plot at the central beam axis of the difference in dose resulting from a -0.8 mm shift in x.

(b) 2D plot at the central beam axis of the difference in dose resulting from a 1% perturbation in MU.

(c) 2D plot at the central beam axis of the difference in dose resulting from a 0.1% perturbation in E.

Figure 4.8: Comparison of the differences in YODA dose caused by perturbing the entire target in x, MU and E.

As seen in Table 4.3, the maximum deviation was 7.498%, and the mean deviation in the target was 0.2139% with a shift of -0.8 mm in the x direction. The difference in the target is small, however there are voxels outside the target that receive a bigger difference. Figure 4.8a shows a 2D plot of the difference in dose for a -0.8 mm shift in x at the central beam axis. Clearly, the biggest difference in dose, shown in Figure 4.8a, is outside the target. Table 4.4 shows the results for a perturbation in the z direction. Here the maximum deviation was 7.512% and the mean deviation in the target was 0.2332% for a shift of 0.8 mm. These results are comparable to the results of a shift in the x direction, as expected. For the 0.8 mm shift in the z direction, once again the biggest differences are outside of the target cube. When perturbing the MU with 1%, the maximum dose difference is 1%, as displayed in Table 4.5. The mean dose difference in the target cube is then 0.9664%. The effect of a 1% difference in MU at the central beam axis is displayed in Figure 4.8b. As expected, the difference in dose is mostly placed inside the target. Table 4.6 shows the results for perturbing the energy. When perturbing the energy with 0.1%, the maximum dose difference is 3.624%, and the mean dose difference in the target is 0.1851%. This can be seen in Figure 4.8c, when perturbing the energy with 0.1%, the dose difference at the central beam axis is mainly just outside the target, therefore the mean difference in dose inside the target is small.

It is not established that, when there is a systematic error in the log file, this would be the same error for every

energy layer. Another experiment was performed where instead of perturbing the whole target with the same perturbation, for every energy layer a random perturbation was added. This random perturbation was selected using a uniform distribution ranging from −0.8 mm to 0.8 mm in x and z, −1% to 1% in MU and −0.1% and 0.1% in energy. The results for this experiment are shown in Table 4.7.

Table 4.7: The effect of perturbing each energy layer randomly on the difference in dose relative to the maximum dose of the unperturbed case.

Perturbated quantity	Mean $\|\Delta D\|$	Max $\|\Delta D\|$	Passing rate
x	$0.1204\% \pm 0.0408\%$	$2.688\% \pm 1.172\%$	100.0%
z	$0.1700\% \pm 0.0324\%$	$3.324\% \pm 1.100\%$	100.0%
MU	$0.2592\% \pm 0.1595\%$	$0.4121\% \pm 0.2162\%$	100.0%
E	$0.4802\% \pm 0.1558\%$	$1.715\% \pm 0.8016\%$	100.0%

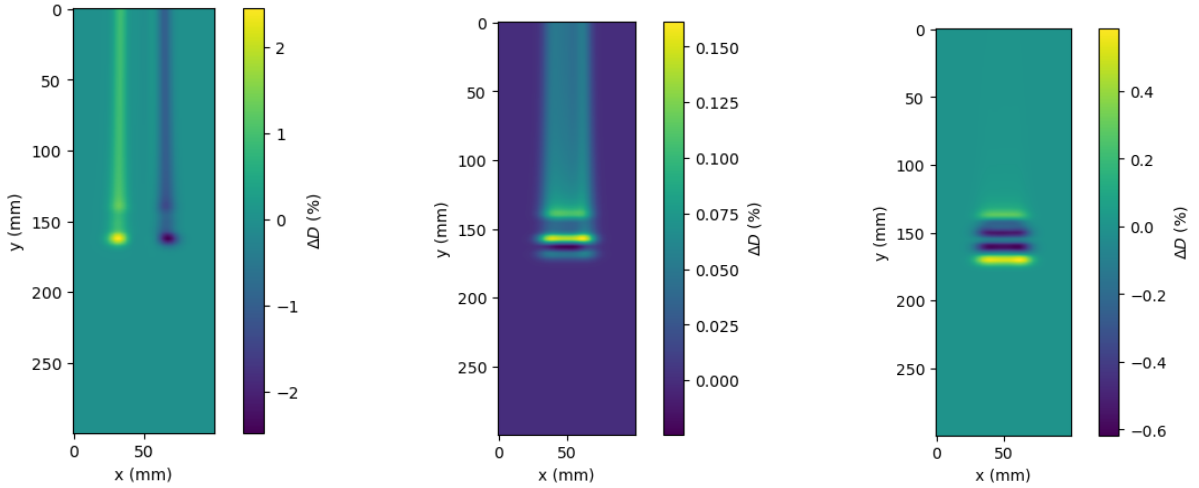

(a) 2D plot at the central beam axis of the difference in dose resulting from random perturbations in x for each energy layer, where mean $|\Delta D|$=0.1067% and max $|\Delta D|$=2.504%

(b) 2D plot at the central beam axis of the difference in dose resulting from random perturbations in MU for each energy layer, where mean $|\Delta D|$=0.07366% and max $|\Delta D|$=0.1729%

(c) 2D plot at the central beam axis of the difference in dose resulting from random perturbations in E for each energy layer, where mean $|\Delta D|$=0.2895% and max $|\Delta D|$= 0.6529%

Figure 4.9: Comparison of the differences in YODA dose caused by randomly perturbing each energy layer in x, MU and E.

Figure 4.9 shows an example of the difference in dose for the perturbations in x, MU and E at the central beam axis from one of the experiments. The difference in dose between the perturbation in x and z can be partly explained by the fact that the perturbations are now randomly selected and therefore there is a difference in these two experiments. Another reason for the difference in x and z is the fact that upon closer examination of the irradiated target cube, the dose is not uniformly deposited. So when perturbing each energy layer with a different perturbation as opposed to the whole cube with the same perturbation, there is a difference in the effect on the dose for perturbing in x or z. When comparing the results of this experiment to the results displayed in Tables 4.3, 4.4, 4.5 and 4.6, only the random perturbations in energy result in a bigger mean difference in the target compared to the previous experiment. This can be explained by the fact that when randomly selecting perturbations in energy for each layer, most of the difference in dose is now inside the cube, whereas while perturbing the whole target in energy most of the difference can be found outside the target. For the perturbations in x,z the differences in dose are comparable to perturbing 0.6 mm to 0.4 mm in the previous experiment. The dose difference in MU found in this experiment is comparable to the case where the whole cube was perturbed with 0.25% in the previous experiment.

Toscano et al. [13] reported a 1% mean dose relative error between the planned dose and the reconstructed dose while comparing a patient plan using a Monte Carlo-based independent algorithm. This error was reduced to almost zero when including their model of systematic and random errors. In the experiment presented in this section, mean relative dose errors smaller than 1% were retrieved when randomly perturbing each energy layer in the spot position. However, these were simple plans in water boxes, without lateral heterogeneities and containing significantly fewer spots than actual patient plans. When there are lateral hetero-

geneities present a small displacement can have a large effect, since the proton beamlet might interact with different types of tissue affecting the final dose distribution significantly. This simple water box model is not extensive enough to be able to compare the results to the publication by Toscano et al. [13]. The experiment should be performed on an actual patient plan before this comparison is possible. Lastly, in this experiment the reference dose was the unperturbed case and not the planned dose, as was the case in the publication by Toscano et al. [13]. Therefore the differences introduced in dose by the limited agreement in the calibration are not considered in this experiment.

When considering the magnitude of the error caused by assuming symmetrical spots found, as found in Subsection 4.3.2, the magnitude of the errors induced by log files are small, as the mean difference in the target cube is an order of magnitude smaller. It should be noted that the difference in spatial spread, used for the investigation of the error induced by assuming beam spot symmetry, was an order of magnitude larger than the perturbations in the spot position used in this experiment.

5

Conclusion and recommendations

Quality assurance is a vital part of proton therapy treatment. When working towards daily adaptive treatment, especially fast-working quality assurance tools are necessary for the workflow. YODA has been proven to be faster than the golden standard Monte Carlo algorithm TOPAS. The aim of this thesis was to investigate how YODA can be calibrated to the clinically used planning system, and which alterations are necessary to be able to use YODA as a patient-specific quality assurance tool. YODA would be used to reconstruct the delivered dose to the patient from log file information, and then compare this to the planned dose. Therefore, the research question was formulated to be, 'How can YODA be calibrated and improved to yield dose distributions that are comparable to clinically generated dose distributions?'. Four steps were taken in this thesis to try to answer this research question and recommendations for further research will be provided.

First, YODA needed to be calibrated to the planning system RayStation. The lowest passing rate found from this calibration was 99.47% for a 190 MeV spot. With this high passing rate, the calibration was successful. An approximation to deal with nuclear interactions was introduced to YODA. A quantity, γ, describing the fraction of locally deposited dose due to nuclear interaction was added in Ψ_{FP} and was optimized at 9 points of mean beam energy. The frequency of which γ is optimized should be investigated, to reduce the computation time of the calibration procedure without lowering the passing rates. To increase the agreement between YODA and RayStation, alternatives to model the nuclear interactions should be investigated. This alternative should not add much computation time to the model, as that would defeat the purpose of the QA application. A proposed alternative could be to use a kernel-based approach to include the effect of secondaries. After the YODA computation is done, a convolution with a dose kernel describing the effect of different secondaries and the proton flux will be performed.

Second, range shifters needed to be included in this calibration, as in patient treatment plans range shifters are often used. This lead to 3 additional BDL files, for a 2 cm, 3 cm and a 5 cm range shifter. The agreement between YODA and RayStation for these cases is comparable to the no range shifter case.

It was discovered that when the beam enters the CT volume under larger gantry angles, the agreement between the RayStation and YODA dose is lower than when entering at a 0° gantry angle. This has two causes. First, because the CT volume was not of the same size in all three axes, there was a difference in the distance from the isocenter to the CT volume surface depending on the gantry angle. RayStation takes this difference into account, however, YODA does not. This resulted in significant differences when irradiating under an angle. This could be solved by making BDL files specifically for the isocenter to CT volume surface distance. A more sophisticated solution would be to define the parameters in the BDL in air at isocenter and then using equations provided by the commissioning procedure for MC^2 [31] to find the parameters at the CT volume surface. This would mean that the calibration procedure has to be adjusted to find the spatial spread, angular spread and correlation at isocenter. A method similar to the commissioning procedure for MC^2 can be used, where the spot size is measured at several depths and the spatial spread, angular spread and correlation at isocenter can be fitted. For the energy, energy spread and number of protons still an optimization procedure can be used. Second, the beam splitting algorithm approximates the beam to be a circle, but when irradiating under an angle the projection of the beam on the CT volume surface will be an ellipse. The beam splitting algorithm

introduces a significant difference when a beam enters the CT volume at the corner. This can be improved by using a larger beam splitting scheme, however, this would slow down computations significantly when considering full patient plans with many more spots than used in this thesis. As the goal was to adapt YODA to be a fast working QA tool, alternatives to the currently used beam splitting algorithm should be investigated. It should be investigated if other splitting schemes, where the subspots are not placed on concentric rings, are more accurate without increasing the number of subspots substantially for angled beams. These two issues need to be solved before an actual patient plan can be tested, because this has a significant influence on the agreement of the YODA and RayStation dose. When there are more beams overlapping with each other, the differences in the RayStation dose and the YODA dose can partly cancel each other out at some voxels. Therefore, it is important to investigate the agreement between YODA and RayStation on full patient plans using the calibrated BDLs.

Third, the effect of assuming symmetrical spots was investigated. This was done by deriving the solution for an asymmetrical spot to the Fermi-Eyges equation. When filling in the symmetrical case in this new solution, some differences were found in the coefficients compared to the currently implemented solution in YODA. Some of these differences seem to have been typos in the solution by Gebäck and Asadzadeh [24], however, it should be investigated if a factor $1/2$ should be included in the $\overline{\Sigma_{tr}}$ term in the Fermi-Eyges equation, and if so, this factor needs to be included in the derivation for the asymmetrical spot solution. The new solution should be implemented in YODA, as there were significant differences found in the integrated Fermi-Eyges flux when assuming a symmetrical spot compared to the asymmetrical spot. This will not be computationally expensive, as it only adds one coefficient to the computation. After this is implemented, the calibration should be performed again, now adding the spatial spread, angular spread and correlation for both lateral directions to the calibration procedure.

Fourth, the effect of a systematic error in the log file was investigated. When looking at the order of magnitude of the errors found in this section compared to the errors found by assuming symmetrical spots, it is clear that first the asymmetry should be implemented. Note that the difference in spatial spread is also an order of magnitude larger than perturbations induced in the spot position. The issues with the angled beams should also be solved before revisiting the effect of systematic log file errors. When these improvements are made, a more extensive investigation of the effect of a log file error on YODA reconstructed dose needs to be done. It could be investigated what the errors are in spot position, MU and energy in a log file at HPTC by performing measurements. From this a model of systematic and random errors dependent on energy, MU and planned spot position can be made following Toscano et al. [13]. A patient plan consisting of multiple beams from different gantry angles can then be reconstructed, using this model to account for realistic errors, and compared to the planned dose. This would give a much more realistic view of the effect of the log file error on the reconstructed dose.

All in all, the creation of the calibration procedure and the calibration of YODA to RayStation was successful. The inclusion of γ has led to a reasonable agreement between YODA and RayStation for higher energies. The optimization procedure can in the future, with simple alterations to, for example, the optimization bounds, be applied to different algorithms and planning systems for certain applications. However, there are improvements necessary before YODA is able to yield dose distributions that are comparable to clinically generated dose distributions and therefore can be used as a patient-specific quality assurance tool. After investigating and implementing the recommendations presented in this chapter the implementation of YODA as this QA tool seems viable and is nearing realization.

Bibliography

[1] Kwf Kankerbestrijding. “Wat we weten over kanker”. In: KWF (Sept. 2023). URL: https://www.kwf.nl/kanker.

[2] Ye Zhang. Application of online image guidance for moving tumour treatment using scanned proton therapy. Jan. 2013. DOI: 10.3929/ethz-a-010158999. URL: http://e-collection.library.ethz.ch/eserv/eth:8651/eth-8651-02.pdf.

[3] Kwangzoo Chung. “A pilot study of the scanning beam quality assurance using machine log files in proton beam therapy”. In: Progress in medical physics 28.3 (Jan. 2017), p. 129. DOI: 10.14316/pmp.2017.28.3.129.

[4] International Atomic Energy Agency. Radiation Oncology Physics. IAEA, Jan. 2005.

[5] Harald Paganetti et al. “Adaptive proton therapy”. In: Physics in Medicine and Biology 66.22 (Nov. 2021), 22TR01. DOI: 10.1088/1361-6560/ac344f.

[6] Chunhua Men, Xun Jia, and Steve. B. Jiang. “GPU-based ultra-fast direct aperture optimization for online adaptive radiation therapy”. In: Physics in medicine biology/Physics in medicine and biology 55.15 (July 2010), pp. 4309–4319. DOI: 10.1088/0031-9155/55/15/008.

[7] Savino Cilla et al. “Template-based automation of treatment planning in advanced radiotherapy: a comprehensive dosimetric and clinical evaluation”. In: Scientific Reports 10.1 (Jan. 2020). DOI: 10.1038/s41598-019-56966-y.

[8] M.F. Belosi et al. “Treatment log files as a tool to identify treatment plan sensitivity to inaccuracies in scanned proton beam delivery”. In: Radiotherapy and Oncology 125.3 (Dec. 2017), pp. 514–519. DOI: 10.1016/j.radonc.2017.09.037.

[9] G. Meier et al. “Independent dose calculations for commissioning, quality assurance and dose reconstruction of PBS proton therapy”. In: Physics in Medicine and Biology 60.7 (Mar. 2015), pp. 2819–2836. DOI: 10.1088/0031-9155/60/7/2819.

[10] Gabriel Guterres Marmitt et al. “Platform for automatic patient quality assurance via Monte Carlo simulations in proton therapy”. In: Physica Medica 70 (Feb. 2020), pp. 49–57. DOI: 10.1016/j.ejmp.2019.12.018.

[11] Steven A. Leibel and Theodore L. Phillips. Textbook of Radiation Oncology. Jan. 2004.

[12] Harald Paganetti and Georges El Fakhri. “Monitoring proton therapy with PET”. In: British Journal of Radiology 88.1051 (July 2015), p. 20150173. DOI: 10.1259/bjr.20150173.

[13] S. Toscano et al. “Impact of machine log-files uncertainties on the quality assurance of proton pencil beam scanning treatment delivery”. In: Physics in Medicine and Biology 64.9 (Apr. 2019), p. 095021. DOI: 10.1088/1361-6560/ab120c.

[14] Carla Winterhalter et al. “Log file based Monte Carlo calculations for proton pencil beam scanning therapy”. In: Physics in Medicine and Biology 64.3 (Jan. 2019), p. 035014. DOI: 10.1088/1361-6560/aaf82d.

[15] Tiberiu Burlacu, Danny Lathouwers, and Zoltán Perkó. “A deterministic Adjoint-Based Semi-Analytical algorithm for fast response change computations in proton therapy”. In: Journal of computational and theoretical transport 52.1 (Jan. 2023), pp. 1–41. DOI: 10.1080/23324309.2023.2166077.

[16] Tiberiu Burlacu, Danny Lathouwers, and Zoltán Perkó. Yet anOther Dose Algorithm (YODA) for independent computations of dose and dose changes due to anatomical changes. Tech. rep. Apr. 2024.

[17] TOPAS tool for particle simulation. URL: https://www.topasmc.org/.

[18] Treatment Planning System - RayStation | RaySearch Laboratories. URL: https://www.raysearchlabs.com/raystation/.

[19] Harald Paganetti. Proton Therapy Physics. CRC Press, Apr. 2016.

[20] Wayne D. Newhauser and R. Zhang. “The physics of proton therapy”. In: Physics in medicine biology/Physics in medicine and biology 60.8 (Mar. 2015), R155–R209. DOI: 10.1088/0031-9155/60/8/r155.

[21] James J. Duderstadt and Louis J. Hamilton. Nuclear reactor analysis. Wiley, Jan. 1991.

[22] H. Edwin Romeijn et al. “A new linear programming approach to radiation therapy treatment planning problems”. In: Operations research 54.2 (Apr. 2006), pp. 201–216. DOI: 10.1287/opre.1050.0261.
[23] Jiajian Shen et al. “Impact of range shifter material on proton pencil beam spot characteristics”. In: Medical physics on CD-ROM/Medical physics 42.3 (Feb. 2015), pp. 1335–1340. DOI: 10.1118/1.4908208.
[24] Tobias Gebäck and Mohammad Asadzadeh. “Analytical Solutions for the Pencil-Beam Equation with Energy Loss and Straggling”. In: Transport theory and statistical physics 41.5-6 (Oct. 2012), pp. 325–336. DOI: 10.1080/00411450.2012.671207.
[25] J Verburg et al. “Automated Monte Carlo simulation of proton therapy treatment plans”. In: Technology in cancer research treatment 15.6 (July 2016), NP35–NP46. DOI: 10.1177/1533034615614139.
[26] Trust-region methods - Cornell University Computational Optimization Open Textbook - Optimization Wiki. URL: https://optimization.cbe.cornell.edu/index.php?title=Trust-region_methods.
[27] Ya-Xiang Yuan. A review of trust region algorithms for optimization. Dec. 2000, pp. 271–282. DOI: 10.1093/oso/9780198505143.003.0023.
[28] minimize(method='trust-constr') — SciPy v1.13.0 Manual. URL: https://docs.scipy.org/doc/scipy/reference/optimize.minimize-trustconstr.html.
[29] Daniel A. Low et al. “A technique for the quantitative evaluation of dose distributions”. In: Medical physics on CD-ROM/Medical physics 25.5 (May 1998), pp. 656–661. DOI: 10.1118/1.598248.
[30] Das S et al. “Gamma Index Analysis as a Patient-Specific Quality Assurance Tool for High-Precision Radiotherapy: A Clinical Perspective of Single Institute Experience”. In: Curēus (Oct. 2022). DOI: 10.7759/cureus.30885.
[31] MCsquare - Commissioning procedure. URL: http://www.openmcsquare.org/documentation_commissioning.html#BDL_format.
[32] Thomas Bortfeld. “An analytical approximation of the Bragg curve for therapeutic proton beams”. In: Medical physics (Lancaster) 24.12 (Dec. 1997), pp. 2024–2033. DOI: 10.1118/1.598116.
[33] S. M. Seltzer. An assessment of the role of charged secondaries from nonelastic nuclear interactions by therapy proton beams in water. Tech. rep. Jan. 1993. DOI: 10.6028/nist.ir.5221.
[34] Martin J. Berger. Penetration of proton beams through water 1. Depth-dose distribution, spectra and LET distribution. Jan. 1993.
[35] Heng Li et al. “Use of treatment log files in spot scanning proton therapy as part of patient-specific quality assurance”. In: Medical physics on CD-ROM/Medical physics 40.2 (Jan. 2013), p. 021703. DOI: 10.1118/1.4773312.
[36] Ozgur Ates et al. “Development of a log file analysis tool for proton patient QA, system performance tracking, and delivered dose reconstruction”. In: Journal of applied clinical medical physics 24.7 (Mar. 2023). DOI: 10.1002/acm2.13972. URL: https://doi.org/10.1002/acm2.13972.
[37] Leonard Eyges. “Multiple Scattering with Energy Loss”. In: Physical review 74.10 (Nov. 1948), pp. 1534–1535. DOI: 10.1103/physrev.74.1534.

A

Solution to the Fermi-Eyges with Gaussian initial condition

In this appendix, the derivation of the asymmetrical spot solution of the Fermi-Eyges equation will be shown. The notation of the dependency of ϕ_{FE} on $(\boldsymbol{r}, \hat{\boldsymbol{\Omega}})$ is dropped in this section to improve readability. Recall that the Fermi-Eyges equation was defined to be [15]

$$\Upsilon(\phi_{FE}) = \frac{\partial \phi_{FE}}{\partial z} + \Omega_x \frac{\partial \phi_{FE}}{\partial x} + \Omega_y \frac{\partial \phi_{FE}}{\partial y} - \overline{\Sigma_{tr}}(z, E_a(z)) \left(\frac{\partial^2 \phi_{FE}}{\partial \Omega_x^2} + \frac{\partial^2 \phi_{FE}}{\partial \Omega_y^2} \right) = 0. \tag{A.1}$$

Separability in the x and y directions can be applied yielding [15]

$$\frac{\partial H(z,\xi,\omega)}{\partial z} + \omega \frac{\partial H(z,\xi,\omega)}{\partial \xi} - \overline{\Sigma_{tr}}(z) \frac{\partial^2 H(z,\xi,\omega)}{\partial \omega^2} = 0, \tag{A.2}$$

where ξ can be either x or y and ω can be either Ω_x or Ω_y. This PDE will be solved using a Gaussian initial condition defined as [15]

$$H(0,\xi,\omega) = C \exp\left(-(a_1 \xi^2 + a_2 \xi\omega + a_3 \omega^2)\right), \tag{A.3}$$

where $a_i, i \in [1,2,3]$ are described by

$$a_1 = \frac{1}{2(1-\varrho^2)\sigma_\xi^2}, \quad a_2 = -\frac{\varrho}{(1-\varrho^2)\sigma_\xi \sigma_\omega}, \quad a_3 = \frac{1}{2(1-\varrho^2)\sigma_\omega^2}. \tag{A.4}$$

To solve Equation A.2, Fourier transforms will be used. The transformation to the Fourier domain can be achieved using the following definition of the Fourier transform

$$\tilde{H}(z,\alpha,\beta) = \frac{1}{2\pi} \int_\infty^\infty H(z,\xi,\omega) \exp\left(-i(\xi\alpha + \omega\beta)\right) \mathrm{d}\xi \mathrm{d}\omega, \tag{A.5}$$

and the inverse transform defined by

$$H(z,\xi,\omega) = \frac{1}{2\pi} \int_\infty^\infty \tilde{H}(z,\alpha,\beta) \exp\left(i(\xi\alpha + \omega\beta)\right) \mathrm{d}\alpha \mathrm{d}\beta. \tag{A.6}$$

Following the work of Eyges [37], the Fourier transform of Equation A.2 resulted in

$$\frac{\partial \tilde{H}}{\partial z} = \alpha \frac{\partial \tilde{H}}{\partial \beta} - \overline{\Sigma_{tr}} \beta^2 \tilde{H}. \tag{A.7}$$

New parameters are introduced to simplify Equation A.7 [37]

$$\begin{aligned} \epsilon &= z + \beta/\alpha, \\ z' &= z. \end{aligned} \tag{A.8}$$

Substitution of these new parameters results in the following equation [37]

$$\frac{\partial \tilde{H}}{\partial z'} = -\alpha^2(\epsilon - z')^2 \overline{\Sigma_{tr}} \tilde{H}. \tag{A.9}$$

This equation yields the solution [37]

$$\tilde{H} = \tilde{G}(\epsilon) \exp\left[-\alpha^2 \int_{\kappa}^{z} (\epsilon - \eta)^2 \overline{\Sigma_{tr}}(\eta) \mathrm{d}\eta\right]. \tag{A.10}$$

A Fourier transform is applied to the initial condition, described in Equation A.3, and yields

$$\tilde{H}(0, \alpha, \beta) = \frac{C}{\sqrt{4a_1a_3 - a_2^2}} \exp\big((a_1\beta^2 - a_2\alpha\beta + a_3\alpha^2)/(a_2^2 - 4a_1a_3)\big). \tag{A.11}$$

This transformed initial condition is subsequently filled in Equation A.10, resulting in

$$\tilde{G}(\beta/\alpha) = \frac{C}{\sqrt{4a_1a_3 - a_2^2}} \exp\big((a_1\beta^2 - a_2\alpha\beta + a_3\alpha^2)/(a_2^2 - 4a_1a_3)\big) \exp\left(\alpha^2 \int_{\kappa}^{0} (\beta/\alpha - \eta)^2] \overline{\Sigma_{tr}}(\eta) \mathrm{d}\eta\right), \tag{A.12}$$

which can also be rewritten as

$$\tilde{G}(\beta/\alpha) = \frac{C}{\sqrt{4a_1a_3 - a_2^2}} \exp\big((a_1\beta^2 - a_2\alpha\beta + a_3\alpha^2)/(a_2^2 - 4a_1a_3)\big) \exp\left(-\alpha^2 \int_{0}^{\kappa} (\beta/\alpha - \eta)^2 \overline{\Sigma_{tr}}(\eta) \mathrm{d}\eta\right). \tag{A.13}$$

This gives the functional form of $\tilde{G}$ and can be filled in Equation A.10. Here β will now be substituted by $\beta + \alpha z$, leading to

$$\begin{aligned} \tilde{H}(z, \alpha, \beta) = &\frac{C}{\sqrt{4a_1a_3 - a_2^2}} \exp\big((a_1(\beta + z\alpha)^2 - a_2\alpha(\beta + z\alpha) + a_3\alpha^2)/(a_2^2 - 4a_1a_3)\big) \\ &\exp\left(-\alpha^2 \int_{0}^{z} (\beta/\alpha + z - \eta)^2 \overline{\Sigma_{tr}}(\eta) \mathrm{d}\eta\right). \end{aligned} \tag{A.14}$$

This solution is then rewritten to be

$$\begin{aligned} \tilde{H}(z, \alpha, \beta) = &\frac{C}{\sqrt{4a_1a_3 - a_2^2}} \exp\big(-(a_1\beta^2 + 2a_1\alpha\beta z - a_2\alpha\beta + a_1\alpha^2 z^2 - a_2\alpha^2 z + a_3\alpha^2)/(4a_1a_3 - a_2^2)\big) \\ &\exp\left(-(\beta^2 \int_{0}^{z} \Sigma_{tr}(\eta) \mathrm{d}\eta + \alpha^2 \int_{0}^{z} (z - \eta)^2 \Sigma_{tr}(\eta) \mathrm{d}\eta + 2\alpha\beta \int_{0}^{z} (z - \eta) \overline{\Sigma_{tr}}(\eta) \mathrm{d}\eta)\right). \end{aligned} \tag{A.15}$$

Introducing some coefficients allows for simplification in Equation A.15. These coefficients are defined to be

$$D = 4a_1a_3 - a_2^2, \tag{A.16}$$

$$A_0(z) = \frac{a_1}{D} + \int_0^z \Sigma_{tr}(\eta)\mathrm{d}\eta, \tag{A.17}$$

$$2A_1(z) = -\frac{a_2}{D} + \frac{2a_1}{D}z + 2\int_0^z (z-\eta)\overline{\Sigma_{tr}}(\eta)\mathrm{d}\eta, \tag{A.18}$$

$$A_2(z) = \frac{a_3}{D} - \frac{a_2}{D}z + \frac{a_1}{D}z^2 + \int_0^z (z-\eta)^2\overline{\Sigma_{tr}}(\eta)\mathrm{d}\eta. \tag{A.19}$$

Substitution the coefficients in Equation A.15 results in the solution

$$\tilde{H}(z,\alpha,\beta) = \frac{C}{\sqrt{D}}\exp\big(-(A_0(z)\beta^2 + 2A_1(z)\alpha\beta + A_2(z)\alpha^2)\big). \tag{A.20}$$

This can then be inversely Fourier transformed back to the ξ,ω domain. Resulting in the one-dimensional solution to the Fermi-Eyges equation

$$H(z,\xi,\omega) = \frac{C}{\sqrt{D}}\frac{\exp\big((A_2(z)\omega^2 - 2A_1(z)\omega\xi + A_0(z)\xi^2)/(4A_1^2(z) - 4A_0(z)A_2(z))\big)}{\sqrt{4A_0(z)A_2(z) - 4A_1^2(z)}}. \tag{A.21}$$

The total solution is described by $\phi_{FE}(\boldsymbol{r},\Omega_x,\Omega_y) = H(z,x,\Omega_x)H(z,y,\Omega_y)$. Mind that for an asymmetrical beam the following coefficients are different for x and y: C, a_1, a_2 and a_3 and therefore $A_0(z)$, $A_1(z)$, $A_2(z)$ and D. Assuming a_1, a_2 and a_3 correspond to x and a_4, a_5 and a_6 correspond to y defined by;

$$a_1 = \frac{1}{2(1-\varrho_x^2)\sigma_x^2}, \quad a_2 = -\frac{\varrho_x}{(1-\varrho_x^2)\sigma_x\sigma_{\Omega_x}}, \quad a_3 = \frac{1}{2(1-\varrho_x^2)\sigma_{\Omega_x}^2}, \tag{A.22}$$

and

$$a_4 = \frac{1}{2(1-\varrho_y^2)\sigma_y^2}, \quad a_5 = -\frac{\varrho_y}{(1-\varrho_y^2)\sigma_y\sigma_{\Omega_y}}, \quad a_6 = \frac{1}{2(1-\varrho_y^2)\sigma_{\Omega_y}^2}. \tag{A.23}$$

The total solution for an asymmetrical beam yields

$$\phi_{FE}(\boldsymbol{r},\hat{\boldsymbol{\Omega}}) = \frac{C_1}{\sqrt{4a_1a_3 - a_2^2}}\frac{C_2}{\sqrt{4a_4a_6 - a_5^2}}\frac{\exp\big((A_2(z)\Omega_x^2 - 2A_1(z)\Omega_x x + A_0(z)x^2)/(4A_1^2(z) - 4A_0(z)A_2(z))\big)}{\sqrt{4A_0(z)A_2(z) - 4A_1^2(z)}\sqrt{4A_3(z)A_5(z) - 4A_4^2(z)}}$$

$$\exp\Big((A_5(z)\Omega_y^2 - 2A_4(z)\Omega_y y + A_3(z)y^2)/(4A_4^2(z) - 4A_3(z)A_5(z))\Big), \tag{A.24}$$

where,

$$A_3(z) = \frac{a_4}{D_2} + \int_0^z \overline{\Sigma_{tr}}(\eta)\mathrm{d}\eta, \tag{A.25}$$

$$2A_4(z) = -\frac{a_5}{D_2} + \frac{2a_4}{D_2}z + 2\int_0^z (z-\eta)\overline{\Sigma_{tr}}(\eta)\mathrm{d}\eta, \tag{A.26}$$

$$A_5(z) = \frac{a_6}{D_2} - \frac{a_4}{D_2}z + \frac{a_5}{D_2}z^2 + \int_0^z (z-\eta)^2\overline{\Sigma_{tr}}(\eta)\mathrm{d}\eta, \tag{A.27}$$

and $D_2 = 4a_4a_6 - a_5^2$.